

PAHs as a tracer of star formation?

E. Peeters

NASA-Ames Research Center, Mail Stop 245-6, Moffett Field, CA 94035, USA

`epeeters@mail.arc.nasa.gov`

H.W.W. Spoon

*Kapteyn Institute, P.O. Box 800, 9700 AV Groningen, The Netherlands;
Cornell University, Astronomy Department, Ithaca, NY 14853, USA*

and

A.G.G.M. Tielens

*SRON National Institute for Space Research/Kapteyn Institute, P.O. Box 800, 9700 AV
Groningen, The Netherlands*

ABSTRACT

Infrared (IR) emission features at 3.3, 6.2, 7.7, 8.6 and $11.3\mu\text{m}$ are generally attributed to IR fluorescence from (mainly) FUV pumped large Polycyclic Aromatic Hydrocarbon (PAH) molecules. As such, these features trace the FUV stellar flux and are thus a measure of star formation. We examined the IR spectral characteristics of Galactic massive star forming regions and of normal and starburst galaxies, as well as AGNs and ULIRGs. The goal of this study is to analyze if PAH features are a good qualitative and/or quantitative tracer of star formation and hence the application of PAH emission as a diagnostic tool in order to identify the dominant processes contributing to the infrared emission from Seyfert's and ULIRGs. We develop a new MIR/FIR diagnostic diagram based upon our Galactic sample and compare it to the diagnostic tools of Genzel et al. (1998) and (Laurent et al. 2000), with these diagnostic tools also applied to our Galactic sample. This MIR/FIR diagnostic is derived from the FIR normalized $6.2\mu\text{m}$ PAH flux and the FIR normalized $6.2\mu\text{m}$ continuum flux. Within this diagram, the Galactic sources form a sequence spanning a range of 3 orders of magnitude in these ratios, ranging from embedded compact H II regions to exposed Photo Dissociation Regions (PDRs) and the (diffuse) ISM. However, the variation in the $6.2\mu\text{m}$ PAH feature-to-continuum ratio is relative small. Comparison

of our extragalactic sample with our Galactic sources revealed an excellent resemblance of normal and starburst galaxies to exposed PDRs. While Seyfert-2's coincide with the starburst trend, Seyfert-1's are displaced by at least a factor 10 in $6.2\,\mu\text{m}$ continuum flux, in accordance with general orientation dependent unification schemes for AGNs. ULIRGs show a diverse spectral appearance. Some show a typical AGN hot dust continuum. More, however, are either starburst-like or show signs of strong dust obscuration in the nucleus. One characteristic of the ULIRGs also seems to be the presence of more prominent FIR emission than either starburst galaxies or AGNs. We discuss the observed variation in the Galactic sample in view of the evolutionary state and the PAH/dust abundance and discuss the use of PAHs as quantitative tracers of star formation activity. Based on these investigations we find that PAHs may be better suited as a tracer of B stars, which dominate the Galactic stellar energy budget, than as a tracer of massive star formation (O stars).

Subject headings: Infrared: ISM: lines and bands – ISM: molecules – Infrared : Galaxies – H II regions – Galaxies: ISM – Galaxies: nuclei

1. Introduction

The mid-infrared (MIR) spectra of many objects with associated dust and gas are dominated by the well-known emission features at 3.3, 6.2, 7.7, 8.6 and $11.2\,\mu\text{m}$ commonly called the unidentified infrared (UIR) bands. These bands are now generally attributed to vibrational emission of Polycyclic Aromatic Hydrocarbons (PAHs) containing $\simeq 50$ carbon atoms (Léger & Puget 1984; Allamandola et al. 1985, 1989; Puget & Léger 1989; Tielens et al. 1999, 2000). One key aspect of these IR emission features is that they are particularly bright in regions illuminated by UV bright, early type stars responsible for H II regions and reflection nebulae (RNe).

With the launch of the Infrared Space Observatory (ISO), a huge amount of IR data became available, revealing the omnipresent nature of these PAH features. By now, these features have been detected in a wide range of objects and environments, from post-AGB stars and planetary nebulae (PNe), to H II regions, RNe, the diffuse interstellar medium (ISM) and extragalactic sources, up to redshifts of $z=0.3$. Various studies of Galactic sources with bright PAH emission features have been performed (see e.g. the ISO special issue, A&A, 315, 1996 and, for a recent review, Peeters et al. (2004)). Of particular importance here are the studies of the PAHs in H II regions, which characterized the UIR bands (and their variations) in massive star forming regions (Verstraete et al. 1996; Van Kerckhoven et al.

2000; Hony et al. 2001; Peeters et al. 2002a; Vermeij et al. 2002; Verstraete et al. 2001; van Diedenhoven et al. 2004).

The MIR extragalactic ISO studies established that PAH emission features in extragalactic environments are very similar to those in Galactic star forming regions (e.g. Genzel et al. 1998; Lutz et al. 1998; Mirabel et al. 1998; Charmandaris et al. 1999; Rigopoulou et al. 1999; Clavel et al. 2000; Helou et al. 2000; Tran et al. 2001). This property has since been used qualitatively and quantitatively as diagnostics for the ultimate physical processes powering Galactic nuclei. In particular, Genzel et al. (1998) found that the $7.7 \mu\text{m}$ PAH feature-to-continuum ratio is on average an order of magnitude smaller for Seyfert 1 galaxies (Sf1's) than for starburst galaxies. Conversely, the ratio of the high- to low-excitation emission lines $[\text{O IV}]/[\text{Ne II}]$ was found to be two orders of magnitude higher for Active Galactic Nuclei (AGNs, both Sf1's and 2's) than for starburst galaxies. These two ratios are therefore used to separate AGNs and starburst galaxies. Ultra-Luminous InfraRed Galaxies (ULIRGs) are found to reside in between the two groups, although closer to the starburst galaxies, indicating that 80% of the ULIRGs are predominantly powered by star formation. A second MIR diagnostic plot was devised by Laurent et al. (2000). This diagram separates H II regions, PDRs and AGN-dominated spectra on the basis of their distinctly different ratio of warm ($15 \mu\text{m}$) to hot ($6 \mu\text{m}$) continuum and the value of their $6.2 \mu\text{m}$ PAH feature-to-continuum ratio. The diagram thereby allows an estimation of the contribution of the AGN, PDRs and H II regions to a given MIR spectrum. Given the absence of MIR emission lines for the majority of ULIRGs, Lutz et al. (1998) adapted the Genzel diagram and replaced the $[\text{OIV}]/[\text{NeII}]$ line ratio by the ratio of 5.9 to $60 \mu\text{m}$ continuum ($5.9/60$ ratio). In this diagram the majority of ULIRGs are found at high PAH feature-to-continuum ratio and low $5.9/60$ ratio, close to the position of starburst galaxies. Fewer ULIRGs are found along the mixing line which extends to pure AGNs, at low PAH feature-to-continuum ratio and high $5.9/60$ ratio. Clavel et al. (2000) compared the MIR spectral properties of Sf1s and Sf2s. They found that the $7.7 \mu\text{m}$ PAH luminosity distributions of both types are the same, indicating that the properties of the host galaxies are unrelated to the type-1/2 classification of the nuclear activity. They also found that, on average, the $7.7 \mu\text{m}$ continuum of Sf2s is a factor ~ 8 weaker than of Sf1s and attribute this to dust obscuration in the nuclear environment, which, in line with the unified models for AGNs (Antonucci 1993), is due to the orientation of the AGN torus. Another result of this study is that except for the emission line spectrum, the $3\text{--}12 \mu\text{m}$ spectra of Sf2s appear very similar to those of normal and starburst galaxies.

The goal of this paper is to establish the characteristics of PAH emission bands in regions of massive star formation in the Milky Way, in order to use them as a tool for studying star formation on a galaxy-wide scale and to apply these tools to the study of extragalactic

starbursts in Seyferts, ULIRGs and QSOs.

Sect. 2 presents MIR observations of a Galactic sample and of a sample of normal, starburst, Seyfert and (ultra-luminous) IR galaxies and QSOs. Their spectral characteristics are discussed in Sect. 3. In Sect. 4, we investigate three IR diagnostic tools designed to distinguish AGN- from starburst-dominated spectra. Sect. 5 highlights the PAH abundance as fraction of the total amount of dust and the application of the PAH emission bands as tracers of star formation. The conclusions are stated in Sect. 6.

2. Observations

2.1. Galactic sample

The sample of H II regions was taken from the Galactic “Ultra Compact H II region” ISO program (Peeters et al. 2002b) complemented with the Orion Bar, M17 and 30 Dor. Only those spectra with sufficient S/N are included in this sample. As a reference, we included RNe, heavily embedded protostars exhibiting PAH emission and the (diffuse) ISM in various regions. For details on the sources and references, see Table 1.

Most spectra were obtained with the Short Wavelength Spectrometer (SWS, de Graauw et al. 1996) on board ISO (Kessler et al. 1996) using the AOT 01 scanning mode at various speeds with resolving power ($\lambda/\Delta\lambda$) ranging from 400 to 1500 (see Table 1). The data were processed with the SWS Interactive Analysis package IA³ (de Graauw et al. 1996) using calibration files and procedures equivalent with pipeline version 10.0 or later. A detailed account of this reduction can be found in Peeters et al. (2002b). We spliced the subbands to form a continuous spectrum from 5 to 15 μm . The amount of shifting between subbands is within the calibration uncertainties for the region of interest and does influence the derived fluxes. A few sources were obtained with ISO-PHT-S, ISO-CAM-CVF, IRTS-MIRS and MSX with resolving power ($\lambda/\Delta\lambda$) of respectively ~ 90 , 35, 30 and 800. We refer to the original papers (see Table 1) for an account of the reduction process.

Table 1. Journal of observations together with the derived fluxes.

Source	α (J2000) ^a	δ (J2000) ^a	Instrument ^b	TDT ^c	Ref.	6.2 PAH ^d	cont. ^d [5.3,5.8]	cont. ^d [6.0,6.5]	cont. ^d [14,15]	FIR ^d	Scaling ^e	Ref. FIR
HII regions												
						W/m ²	W/m ²	W/m ²	W/m ²	W/m ²		
W 3A 02219+6125 ^f	02 25 44.59	+62 06 11.20	ISO-SWS 01(2)	64600609	1	2.16(-13)	3.77(-13)	4.99(-13)	4.04(-12)	1.56(-09)	0.33	1
			ISO-SWS 01(2)	78800709	1	2.36(-13)	3.38(-13)	4.87(-13)	4.38(-12)	1.56(-09)	0.33	1
30 Dor	05 38 46.00	-69 05 07.91	ISO-SWS 01(4)	17100512	2	2.61(-14)	7.18(-14)	4.84(-14)	3.08(-13)	5.75(-11)	0.29	18
OrionBar D8	05 35 18.22	-05 24 39.89	ISO-SWS 01(2)	69501409	3	3.16(-13)	2.05(-13)	3.30(-13)	1.72(-12)	-		
OrionBar BRGA	05 35 19.31	-05 24 59.90	ISO-SWS 01(2)	69502108	-	3.76(-13)	2.10(-13)	3.31(-13)	1.07(-12)	-		
OrionBar D5	05 35 19.81	-05 25 09.98	ISO-SWS 01(2)	83101507	-	5.44(-13)	2.34(-13)	3.82(-13)	1.01(-12)	3.50(-11)	-	19
OrionBar H2S1	05 35 20.31	-05 25 19.99	ISO-SWS 01(2)	69501806	4	3.47(-13)	1.89(-13)	3.04(-13)	6.94(-13)	-		
OrionBar D2	05 35 21.40	-05 25 40.12	ISO-SWS 01(2)	69502005	-	1.20(-13)	9.23(-14)	1.20(-13)	4.67(-13)	-		
Orion	centered on Trapezium		MSX	-	5	1.77(-5) ^g	6.50(-06) ^g	1.51(-5) ^g	5.52(-05) ^g	2.80(-3) ^{g,h}	-	20
IRAS 10589-6034	11 00 59.78	-60 50 27.10	ISO-SWS 01(2)	26800760	1	1.28(-13)	1.05(-13)	1.38(-13)	4.46(-13)	1.47(-10)	0.74	1
IRAS 12063-6259	12 09 01.15	-63 15 54.68	ISO-SWS 01(2)	25901414	1	1.18(-13)	1.57(-13)	1.96(-13)	5.79(-13)	1.60(-10)	0.81	1
IRAS 12073-6233 ^f	12 10 00.32	-62 49 56.50	ISO-SWS 01(2)	25901572	1	7.76(-14)	5.14(-13)	6.12(-13)	7.75(-12)	1.10(-09)	0.44	1
IRAS 12331-6134 ^f	12 36 01.9	-61 51 03.9	ISO-SWS 01(2)	29900470	1	3.57(-14)	4.32(-14)	5.47(-14)	1.52(-13)	1.34(-10)	0.18	1
IRAS 15384-5348 ^f	15 42 17.16	-53 58 31.51	ISO-SWS 01(2)	29900661	1	3.26(-13)	1.53(-13)	2.55(-13)	6.50(-13)	4.43(-10)	0.50	1
IRAS 15502-5302	15 54 05.99	-53 11 36.38	ISO-SWS 01(2)	27301117	1	9.90(-14)	2.32(-13)	2.88(-13)	9.73(-13)	8.53(-10)	0.63	1
IRAS 16128-5109 ^f	16 16 39.3	-51 16 58.3	ISO-SWS 01(2)	29402233	1	8.48(-14)	7.20(-14)	8.13(-14)	2.23(-13)	5.33(-10)	0.21	1
IRAS 17160-3707 ^f	17 19 26.1	-37 10 53.8	ISO-SWS 01(2)	32400821	1	4.37(-14)	5.54(-14)	6.82(-14)	1.45(-13)	3.51(-10)	0.25	1
IRAS 17221-3619 ^f	17 25 31.7	-36 21 53.5	ISO-SWS 01(2)	33100380	1	7.46(-14)	5.36(-14)	7.24(-14)	2.38(-13)	2.08(-10)	0.23	1
IRAS 17279-3350 ^f	17 31 18.0	-33 52 49.4	ISO-SWS 01(2)	32200877	1	9.74(-14)	5.88(-14)	8.29(-14)	2.31(-13)	1.28(-10)	0.35	1
Sgr C ^f	17 44 35.6	-29 27 29.3	ISO-SWS 01(2)	84100301	1	6.79(-14)	3.82(-14)	2.72(-14)	2.19(-13)	-	-	
IRAS 17455-2800	17 48 41.5	-28 01 38.3	ISO-SWS 01(2)	28701327	1	1.15(-13)	1.24(-13)	1.81(-13)	1.03(-12)	2.29(-10)	0.53	1
IRAS 17591-2228	18 02 13.2	-22 27 58.9	ISO-SWS 01(2)	51500580	1	2.70(-14)	4.89(-14)	4.19(-14)	9.10(-14)	7.26(-11)	0.57	1
IRAS 18032-2032	18 06 13.93	-20 31 43.28	ISO-SWS 01(2)	51500478	1	1.09(-13)	7.88(-14)	1.03(-13)	3.53(-13)	3.19(-10)	0.54	1
IRAS 18116-1646	18 14 35.29	-16 45 20.99	ISO-SWS 01(2)	70300302	1	1.62(-13)	4.58(-14)	1.01(-13)	4.23(-13)	2.94(-10)	0.39	1
GGD -27 ILL ⁱ	18 19 12.00	-20 47 31.10	ISO-SWS 01(2)	14802136	1,6	1.37(-13)	2.81(-13)	2.88(-13)	5.21(-13)	2.16(-10)	1.	1
M17 iram pos. 1	18 20 28.98	-16 11 50.78	ISO-SWS 01(2)	10201811	7	7.54(-14)	9.74(-14)	1.57(-13)	1.99(-12)	4.82(-11)	-	21
M17 iram pos. 2	18 20 27.59	-16 12 0.90	ISO-SWS 01(2)	09900212	7	4.48(-14)	1.44(-13)	3.05(-13)	4.07(-12)	-	-	
M17 iram pos. 3	18 20 26.19	-16 12 11.02	ISO-SWS 01(2)	09901413	7	1.20(-13)	1.59(-13)	2.18(-13)	3.21(-12)	-	-	
M17 iram pos. 4	18 20 24.79	-16 12 21.10	ISO-SWS 01(2)	09900214	7	3.35(-13)	1.59(-13)	2.49(-13)	1.28(-12)	-	-	
M17 iram pos. 5	18 20 23.40	-16 12 31.21	ISO-SWS 01(2)	09901415	7	2.68(-13)	1.46(-13)	2.02(-13)	4.54(-13)	-	-	
M17 iram pos. 6	18 20 22.09	-16 12 41.29	ISO-SWS 01(2)	09900216	7	2.03(-13)	8.34(-14)	1.51(-13)	2.26(-13)	-	-	

Table 1—Continued

Source	α (J2000) ^a	δ (J2000) ^a	Instrument ^b	TDT ^c	Ref.	6.2 PAH ^d	cont. ^d [5.3,5.8]	cont. ^d [6.0,6.5]	cont. ^d [14,15]	FIR ^d	Scaling ^e	Ref. FIR
M17 iram pos. 7	18 20 20.70	−16 12 51.41	ISO-SWS 01(2)	32900866	7	2.05(-13)	1.03(-13)	1.52(-13)	1.81(-13)	-	-	
M17 iram pos. 8	18 20 19.31	−16 13 01.49	ISO-SWS 01(2)	09901417	7	5.81(-14)	2.11(-14)	2.98(-14)	8.30(-14)	-	-	21
M17 North	18 20 32.77	−16 01 42.49	ISO-SWS 01(2)	09901105	8	7.01(-14)	1.03(-13)	1.38(-13)	1.03(-13)	1.45(-10)	0.23	
IRAS 18317−0757	18 34 24.94	−07 54 47.92	ISO-SWS 01(2)	47801040	1	2.93(-13)	1.51(-13)	2.55(-13)	7.28(-13)	1.97(-10)	0.78	1
IRAS 18434−0242	18 46 04.09	−02 39 20.02	ISO-SWS 01(2)	15201383	1,6	1.88(-13)	3.58(-13)	5.11(-13)	4.41(-12)	6.98(-10)	0.92	1
IRAS 18469−0132	18 49 33.0	−01 29 03.70	ISO-SWS 01(2)	71100888	1	7.63(-14)	6.59(-14)	6.78(-14)	2.11(-13)	1.26(-10)	0.66	1
IRAS 18479−0005	18 50 30.8	−00 01 59.40	ISO-SWS 01(2)	15201791	1	3.05(-14)	9.97(-14)	9.47(-14)	5.81(-13)	2.79(-10)	0.77	1
IRAS 18502+0051	18 52 50.21	+00 55 27.59	ISO-SWS 01(2)	15201645	1	1.08(-13)	9.13(-14)	8.66(-14)	5.91(-13)	1.25(-10)	0.86	1
IRAS 19207+1410 ^f	19 23 02.4	+14 16 40.60	ISO-SWS 01(2)	15001041	1	6.05(-14)	6.22(-14)	5.12(-14)	2.95(-13)	3.79(-10)	0.28	1
IRAS 19442+2427 ^{i?}	19 46 20.09	+24 35 29.40	ISO-SWS 01(2)	15000444	1,6	2.54(-13)	2.46(-13)	2.98(-13)	6.24(-13)	2.71(-10)	0.68	1
IRAS 19598+3324 ⁱ	20 01 45.6	+33 32 43.70	ISO-SWS 01(4)	38402466	1	1.41(-13)	2.22(-12)	2.32(-12)	7.53(-12)	8.89(-10)	0.90	1
IRAS 21190+5140	21 20 44.89	+51 53 26.99	ISO-SWS 01(2)	15901853	1	9.38(-14)	9.06(-14)	1.10(-13)	8.92(-13)	8.66(-11)	1.	1
IRAS 22308+5812	22 32 45.95	+58 28 21.00	ISO-SWS 01(2)	17701258	1,6	1.14(-13)	8.18(-14)	1.12(-13)	1.63(-13)	7.39(-11)	0.72	1
				56101082	1	1.31(-13)	8.03(-14)	1.17(-13)	1.22(-13)	7.39(-11)	0.72	1
IRAS 23030+5958	23 05 10.60	+60 14 40.99	ISO-SWS 01(2)	22000961	1	7.79(-14)	7.59(-14)	8.54(-14)	2.09(-13)	1.25(-10)	0.57	1
IRAS 23133+6050	23 15 31.39	+61 07 08.00	ISO-SWS 01(2)	22001506	1	2.45(-13)	1.37(-13)	2.13(-13)	4.92(-13)	1.96(-10)	0.98	1
Reflection Nebulae												
NGC 7023 I ^f	21 01 31.90	+68 10 22.12	ISO-SWS 01(4)	20700801	9	1.58(-13)	9.61(-14)	8.51(-14)	3.72(-14)	3.46(-11)	0.38	22
NGC 2023 ^f	05 41 38.29	−02 16 32.59	ISO-SWS 01(2)	65602309	10	8.28(-14)	5.64(-14)	4.67(-14)	2.43(-14)	3.04(-12)	-	23
Embedded protostars												
NGC7538 IRS1	23 13 45.27	+61 28 09.98	ISO-SWS 01(3)	38501842	11	2.17(-13)	4.01(-12)	4.06(-12)	5.98(-12)	1.80(-10)	-	24
MONR2 IRS2	06 07 45.79	−06 22 50.02	ISO-SWS 01(1)	71102004	-	4.82(-13)	2.77(-12)	2.60(-12)	1.97(-12)	-	-	
Interstellar Medium line-of-sights												
Galatic Center SgrA*	17 45 39.97	−29 00 28.70	ISO-SWS 01(4)	09401801	12	9.69(-14)	4.80(-12)		2.34(-11)	-	-	
Galatic Center Ring NE	17 45 41.80	−28 59 50.50	ISO-SWS 01(4)	09500203	13	8.28(-14)	1.08(-13)		4.91(-13)	-	-	
						W/m ² /sr	W/m ² /sr	W/m ² /sr	W/m ² /sr	W/m ² /sr		

Table 1—Continued

Source	α (J2000) ^a	δ (J2000) ^a	Instrument ^b	TDT ^c	Ref.	6.2 PAH ^d	cont. ^d [5.3,5.8]	cont. ^d [6.0,6.5]	cont. ^d [14,15]	FIR ^d	Scaling ^e	Ref. FIR
Rho-Oph	16 25 41.09	−24 06 46.90	ISO-CAM 04	09202119	14	3.74(-07)	1.15(-07)	3.98(-07)	1.66(-07)	2.61(-05)	-	14
SMC B1 # 1 cloud	00 45 32.50	−73 18 16.30	ISO-CAM 04	23200127 68602088	15	2.29(-08)	7.54(-09)	6.50(-09)	1.18(-09)	<0.46(-06)	-	15
Milky Way - ISM (average)			ISO-PHOT-S	-	16	3.72(-07)	2.17(-12)	2.61(-07)	-	32.30(-06)	-	15
NGC891 (average within 144'' from center)			ISO-PHOT-S	-	16	3.72(-07)	2.17(-12)	2.61(-07)	-	13.00(-06)	-	16
DISM 1	$44^\circ \leq l \leq 44^\circ 40', -0^\circ 40' \leq b \leq 0^\circ$		IRTS	-	17	1.31(-07)	1.51(-07)	2.44(-07)	-	23.00(-06)	-	17
DISM 2	$50^\circ \leq l \leq 53^\circ, 1^\circ \leq b < 2^\circ$		IRTS	-	17	5.14(-08)	8.23(-08)	1.35(-07)	-	10.00(-06)	-	17
DISM 3	$51^\circ \leq l \leq 54^\circ, 2^\circ \leq b \leq 3^\circ$		IRTS	-	17	2.00(-08)	1.90(-08)	4.81(-08)	-	6.50(-06)	-	17

^aUnits of α are hours, minutes, and seconds, and units of δ are degrees, arc minutes, and arc seconds.

^bSWS observing mode used (see de Graauw et al. 1996). Numbers in brackets correspond to the scanning speed.

^cEach ISO observation is given a unique TDT (Target Dedicated Time) number.

^dSee text for details. Uncertainties on the MIR fluxes less than 20%

^eFIR Scaling factor, see text for details.

^fMIR/FIR ratio influenced by beam effects, confusion with other sources or mispointings (Peeters et al. 2002a; Martín-Hernández et al. 2003).

^gIn units of W/m²/sr.

^hThe contribution of IRC2 and BN is estimated on 4(4)L_☉ (Thronson et al. 1986) and subtracted from the observed FIR luminosity.

ⁱWater ice absorption (6 μ m) present (Peeters et al. 2002a).

References. — 1 : Peeters et al. (2002b); 2 : Sturm et al. (2000) 3 : Cesarsky et al. (2000); 4 : Verstraete et al. (2001); 5 : Simpson et al. (1998); 6 : Roelfsema et al. (1996); 7 : Verstraete et al. (1996); 8 : Henning et al. (1998); 9 : Moutou et al. (1999a); 10 : Moutou et al. (1999b); 11 : Gerakines et al. (1999); 12 : Lutz et al. (1996) 13 : Lutz et al. (1999) 14 : Boulanger et al. (1996) 15 : Kahanpää et al. (2003); 16 : Reach et al. (2000); 17 : Onaka et al. (1996); 18 : Vermeij et al. (2002); 19 : Werner et al. (1976); 20 : Thronson et al. (1984); 21 : Meixner et al. (1992); 22 : Casey (1991); 23 : Steiman-Cameron et al. (1997); 24 : Thronson & Harper (1979)

2.2. ISO galaxy sample

The MIR galaxy spectra presented here have been drawn from our database of some 250 ISO galaxy spectra, described in Spoon et al. (2002). The sample comprises normal galaxies, starburst galaxies, Seyfert galaxies, QSOs, LIRGs, ULIRGs and Hyper Luminous IR Galaxies (HyLIRGs). Depending on the size of the aperture used and the distance to the source, the spectra probe physical sizes ranging from 73 pc ($4.5''$) for the nearest source (Cen A; $D=3.5$ Mpc) and the entire disk (assuming $R_{\text{disk}}=10$ kpc) for galaxies beyond 170 Mpc. The MIR spectra are supplemented with IR photometry from the IRAS Faint Source Catalog (FSC). Given a beam size of $\sim 60''$, the physical sizes probed by IRAS range from 1 kpc for the nearest source and the entire disk for galaxies beyond 73 Mpc. For details on the data reduction, see Spoon et al. (2002).

3. The spectral characteristics

In this section, we focuss on the spectral characteristics of our sample sources in a qualitative way. A quantitative description is given in Sect. 4 and 5.

3.1. H II regions and ISM

Fig. 1 (b – e) shows the MIR spectra of a few H II regions, carefully selected to span the range from highly embedded H II regions (e.g. W3) to optically visible H II regions (e.g. Orion). These spectra are characterized by a strong rising dust continuum due to thermal dust emission, corresponding to dust temperatures of ~ 60 – 70 K. Many H II regions also show strong continuum emission at $\lambda < 12 \mu\text{m}$, whose origin is unclear. Possibly, this continuum is due to a small fraction of dust inside the H II region, heated to high temperatures by resonantly scattered $\text{Ly}\alpha$ radiation. Alternatively, these are larger (~ 500 C-atoms) PAH-like structures stochastically heated by a single or multi-photon event. On top of the dust continuum, there is a series of fine-structure lines and hydrogen recombination lines. In addition, these spectra exhibit prominent PAH emission features, often silicate absorption and in some cases absorption bands due to molecular ice species (CO_2 , H_2O).

In contrast, RNe exhibit a much weaker dust continuum indicating lower dust temperatures, strong PAH emission and no fine-structure lines or recombination lines (Fig. 1 f). A peculiar spectrum is that of the heavily obscured H II region K3–50A, showing all characteristics of H II regions except for the dust continuum which is more similar to that of massive protostars (Fig. 1 a). This source also exhibits a multitude of ice absorption features

(Peeters et al. 2002b).

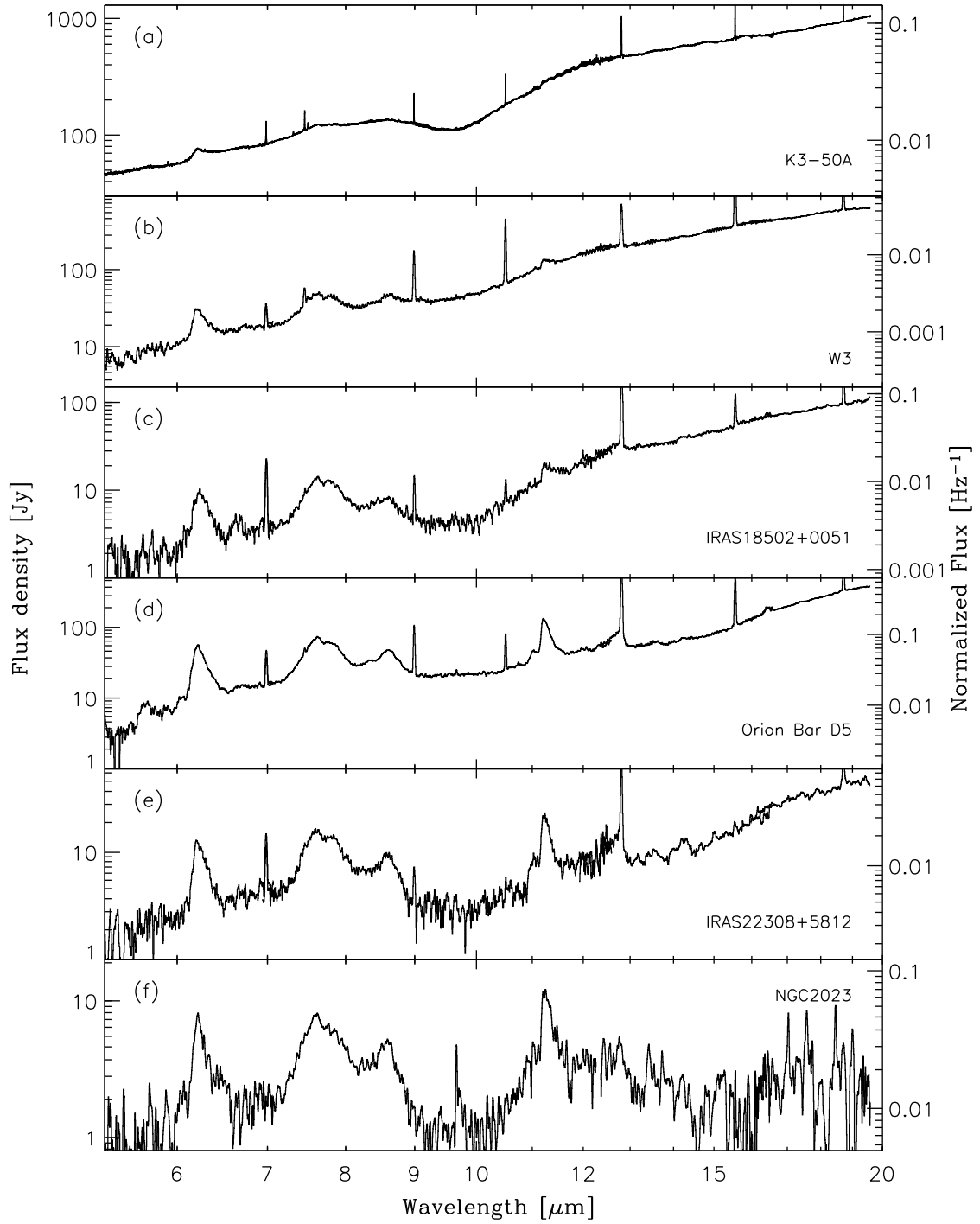


Fig. 1.— Spectral variation in the MIR characteristics of H II regions (for 2–200 μm spectra, see Peeters et al. 2002b). As a reference, the RN NGC2023 is shown in the bottom panel. The units on the right vertical axis represent the FIR normalized flux.

Each of these emission/absorption components characteristic of H II regions is influenced by the local physical conditions and hence, although their global characteristics are very similar, the individual sources display great diversity in their spectral properties (for this sample see Roelfsema et al. 1996; Verstraete et al. 1996, 2001; Hony et al. 2001; Peeters et al. 2002a,b; Martín-Hernández et al. 2002; Vermeij et al. 2002; van Dienenhoven et al. 2004). Indeed, large variations are present in the relative strength of the PAH emission bands and the dust continuum at various wavelengths (Fig. 1). While the PAH features are relatively weak compared to the continua in the spectra presented in the top panels, the opposite is true for the spectra in the lower panels, indicating a smooth trend among the H II regions, ultimately going to that of RNe. However, the strength of the thermal emission of dust below $20\ \mu\text{m}$ is highly influenced by the dust temperature and the amount of dust. Indeed, when normalized on the far-infrared (FIR) flux (Fig. 1 : right y-axis), the sequence of sources going from low to high relative strength of PAH over FIR dust continuum ratio is different, but, here as well, going toward the high ratios of RNe. Both PAH to continuum ratios (i.e. PAH emission with respect to both MIR and FIR continua) vary from highly embedded ultra-compact H II regions (e.g. W3) toward extended optically visible H II regions (e.g. Orion) and ultimately toward RNe (e.g. NGC 2023).

Similarly, the ratio of PAH over hot continuum (e.g. around $\sim 6\ \mu\text{m}$) changes, albeit over a small range. The latter ratio can be influenced by the possible presence of a broad emission plateau underneath the 6.2, 7.7 and $8.6\ \mu\text{m}$ PAH bands of variable strength, sometimes rivaling the strength of the dust continuum at this wavelength. This emission plateau starts longwards of $\sim 6\ \mu\text{m}$ and extends up to $\sim 9\ \mu\text{m}$.

The profile and position of the PAH bands in H II regions and RNe show very little variation from source to source (Peeters et al. 2002a; van Dienenhoven et al. 2004), although spatially within a source differences have been observed (Bregman & Temi 2004, Joblin et al., in prep.). The relative strength of the PAH bands and the fraction of the total PAH flux emitted in each individual band, varies significantly from source to source and spatially within a source. This is very clear when e.g. comparing the 6.2/11.2 PAH ratio for IRAS 18502 and the Orion Bar (for a detailed discussion, see e.g. Verstraete et al. 1996; Joblin et al. 2000; Hony et al. 2001; Vermeij et al. 2002; Peeters et al. 2002a, 2004).

Clearly, the detailed spectral characteristics of H II regions varies and hence no “typical” spectrum exists when considering relative strengths of different emission/absorption components. Since this is partly due to the inclusion of emission of the surrounding Photo Dissociation Region (PDR) and molecular cloud in the aperture, many authors (e.g. Laurent et al. 2000; Sturm et al. 2000) have considered the spectrum of starforming regions where

continuum emission at $15\ \mu\text{m}$ is dominant (e.g. M17) as the typical MIR spectrum for the H II region itself, and a reflection nebula (e.g. NGC 7023) as the typical MIR spectrum of a PDR. Indeed, the PDRs associated with compact H II regions, such as Orion, dominate the PAH emission from the region as a whole (Chrysostomou et al. 1992; Giard et al. 1992, 1994; Graham et al. 1993; Sellgren et al. 1990; Tielens et al. 1993; Verstraete et al. 1996; Contursi et al. 1998). The spectra of H II regions measured within a large beam are then considered to be a combination of these two typical spectra. However, some highly embedded H II regions have a distinct dust continuum (Fig. 1) and therefore are not taken into account in this decomposition. Sect. 4 discusses to which extent this decomposition is valid.

3.2. Galaxy sample

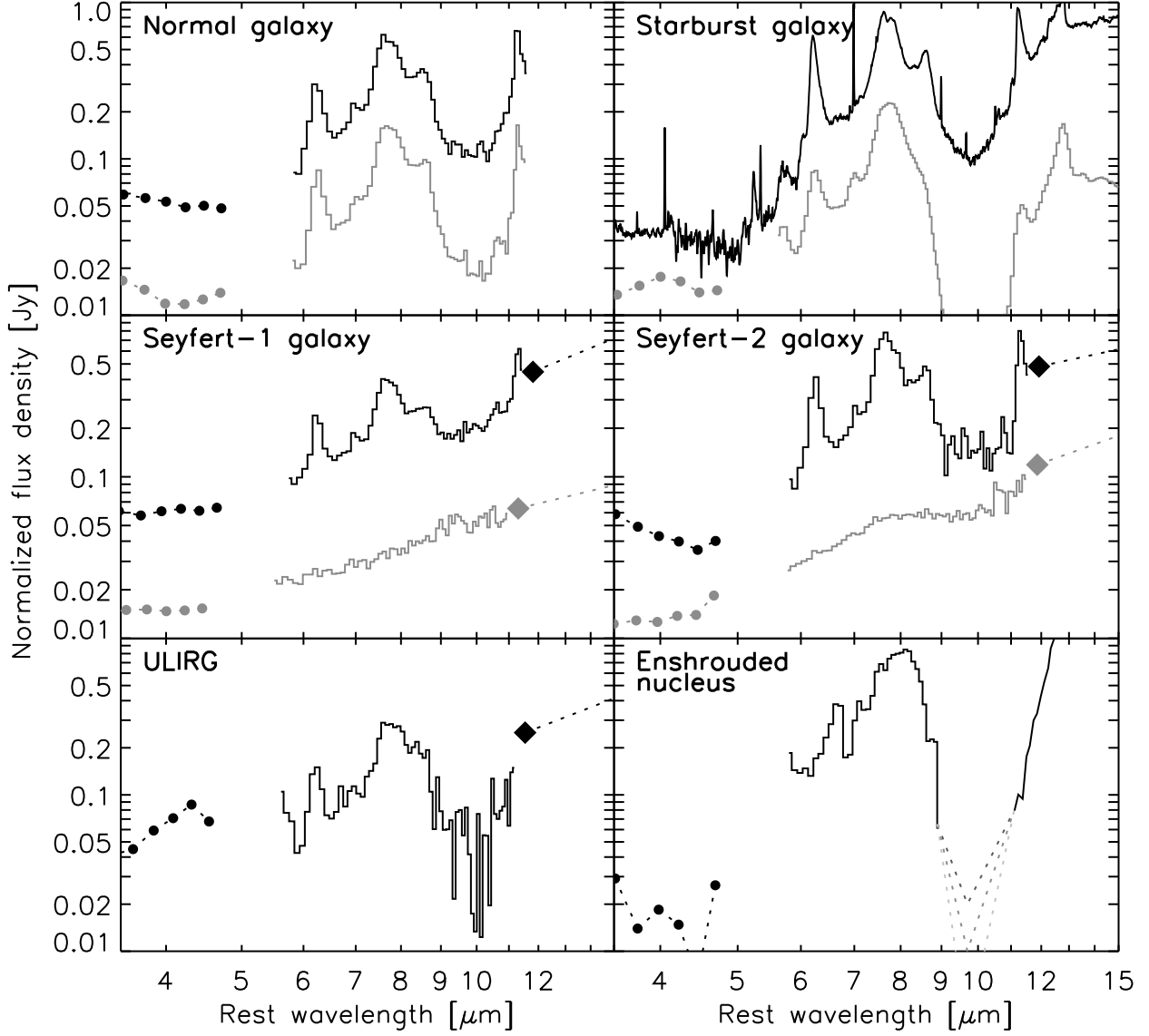


Fig. 2.— MIR galaxy spectra. Dots represent ISO-PHT-SS spectra rebinned to a lower resolution, diamonds the IRAS 12 μm flux shown only when no aperture flux mismatches are seen between ISO and IRAS (see Sect. 4.1). For ease of presentation, the spectra are divided by an arbitrary factor given after each source. **Top-left panel:** The ‘normal’ galaxies NGC 4102 (3, *black*) and NGC 3620 (10, *grey*). **Top-right panel:** The nuclei of the starburst galaxies M82 (45, *black*) and NGC 4945 (25, *grey*). **Mid-left panel:** The Sf1 galaxies NGC 7469 (3, *black*) and IZw 1 (8, *grey*). **Mid-right panel:** The Sf2 galaxies NGC 5953 (1.1, *black*) and PKS 2048–57 (9, *grey*). **Bottom-left panel:** The ultra-luminous IR galaxy UGC 5101 (1). **Bottom-right panel:** The heavily obscured nucleus of NGC 4418 (1.2).

The MIR spectra of normal and starburst galaxies reveal the same spectral features that constitute the spectra of Galactic star forming regions. Invariably, the 6–12 μm range is dominated by the PAH bands at 6.2, 7.7, 8.6 and 11.2 μm (Fig. 2). Beyond 9 μm , starburst galaxies show the additional presence of a warm dust continuum, which is weak or absent in normal galaxies. High resolution spectra also reveal many strong emission lines.

The detailed characteristics of the IR spectra depend on the properties of the galaxy in a way which is not completely understood. In particular, some starburst galaxies also show evidence for the presence of cold, absorbing dust in the nuclear region. A clear example of this is NGC 4945 (top-right, Fig 2), as can be deduced from the weakness of the continuum and PAH features closest to the center of the 9.7 μm silicate absorption feature.

Galaxies optically classified as Seyferts contain an AGN – a massive central black hole, surrounded by an X-ray emitting accretion disk. The disk is believed to be surrounded by a thick molecular torus, the orientation of which determines the Seyfert subtype. Sf1s offer a direct line of sight to the accretion disk and the hot dust at the inner face of the molecular torus. For Sf2s, this direct view is blocked by the torus. Gas above the plane of the torus, highly ionized by the X-rays from the accretion disk, serves to betray the presence of the AGN. The MIR spectra of Seyferts are quite diverse, with some spectra bearing close resemblance to those of starburst galaxies, while other spectra are dominated by a hot dust power law spectrum (middle panels, Fig. 2). Although the average Sf1 spectrum is continuum-dominated and the average Sf2 galaxy spectrum is not (Clavel et al. 2000), our ISO spectral library contains many examples of Seyfert spectra showing the properties of the converse subtype (middle panels, Fig. 2). Evidently, the overall MIR spectral appearance cannot be just the result of the orientation of the AGN torus, but likely also depends on the properties of the host galaxy (i.e. inclination, degree of starburst activity) as well as the power of the central engine. The spatial scale of the observations is another factor determining the MIR spectral appearance of AGNs. Observations of nearby PAH dominated Sf2s, like Circinus and Cen A, have shown the spectrum of the inner 70–150 pc to be dramatically different from the spectrum of the entire galaxy, revealing an underlying, silicate-absorbed, hot dust continuum, likely associated with the AGN (Laurent et al. 2000).

A very different MIR spectrum is detected towards the nucleus of the luminous IR galaxy NGC 4418 (bottom-right, Fig. 2). The spectrum is characterized by a prominent broad peak, centered at 8 μm , too wide and too far displaced to be attributed to 7.7 μm PAH band. Instead, the spectrum appears to be the result of the absorption of a featureless continuum by ices and silicates, both shortward and longward of 8 μm , reminiscent of the spectrum of a deeply embedded protostar (Spoon et al. 2001). MIR imaging has further revealed the source of the absorbed MIR continuum to be extremely compact (<80 pc; Evans et al. 2003) and to

be responsible for most of the IR luminosity. In the absence of any spectral line information, the nature of the nuclear energy source is unclear and may either be extremely dense star formation or AGN activity or a combination of both (e.g. Spoon et al. 2001; Evans et al. 2003). Several other galaxies have been found with spectra similar to NGC 4418, most of them are ULIRGs (Spoon et al. 2002).

The MIR spectra of ULIRGs are more complicated than the spectra of other galaxies due to the presence of copious amounts of dust in their nuclear regions, leading to strong absorption features which may spectrally distort any emission component. Fig. 3 shows a compilation of available HyLIRG and ULIRG spectra, sorted by IR luminosity. While most low-luminosity ULIRGs are dominated by PAH features, the spectra at the high-luminosity end bear close resemblance to AGN hot dust continua, showing little or no sign of PAH features. At intermediate luminosities some ULIRG spectra are PAH dominated, while others show signs of the presence of an NGC 4418-like broad $8\mu\text{m}$ peak, indicating the presence of deeply enshrouded power sources. In addition, some of these ULIRGs show absorptions of water ice (Spoon et al. 2002). A typical, PAH dominated, ULIRG spectrum is further displayed in the lower-left panel of Fig. 2.

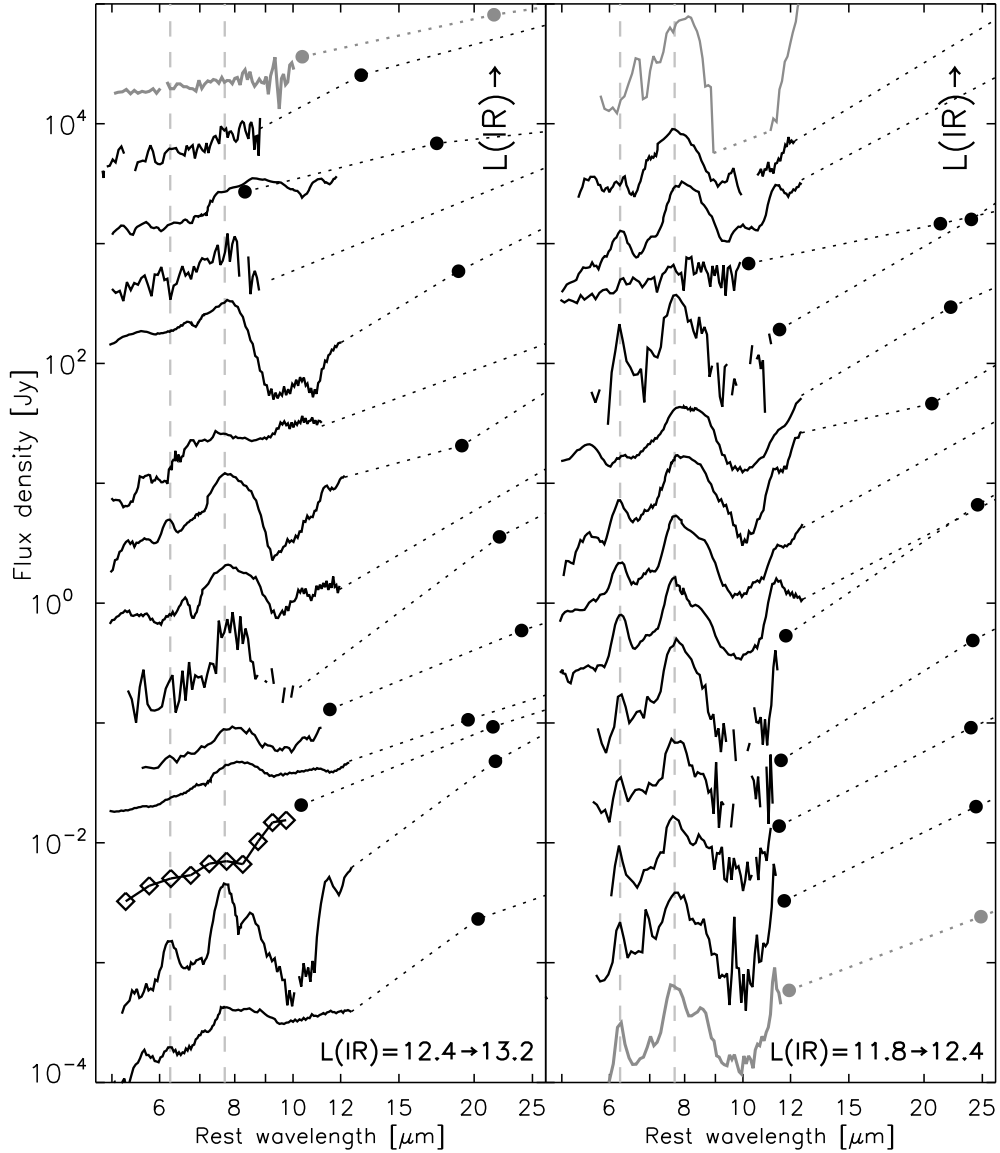


Fig. 3.— HyLIRG and ULIRG spectra sorted by increasing IR luminosity. *Vertical lines* indicate the central wavelengths of the $6.2\,\mu\text{m}$ and $7.7\,\mu\text{m}$ PAH features and *solid circles* the IRAS 12 and 25 μm fluxes (when not an upperlimit). The spectra shown in *grey* serve as template spectra for AGNs (**top-left**), starbursts (**bottom-right**) and deeply enshrouded nuclei (**top-right**). The spectra in the **left panel** are, from top to bottom: 3C 273, 15307+3252, 09104+4109, 00397–1312, 00183–7111, 23529–2119, 03538–6432, 23515–2917, 03158+4227, Mrk 231, 00275–2859, Mrk 1014, 03521+0028 and 22192–3211. In the **right panel**: NGC 4418, 17463+5806, 03000–2719, 23060+0505, 17208–0014, 00188–0856, 04384–4848, 02113–2937, 18030+0705, Arp 220, Mrk 273, 23128–5919, NGC 6240 and NGC 7552.

4. Diagnostic tools to distinguish AGNs and starbursts

As AGNs and star forming regions have distinct spectral characteristics, their relative contribution to observed MIR spectra can be determined in various ways. In this section, we focus on three different diagnostic tools, all based on the strength of PAH bands.

4.1. A MIR/FIR diagnostic

Indicative of regions predominantly powered by star formation are the strong PAH bands. As a measure of the strength of these PAH bands, we prefer the $6.2\,\mu\text{m}$ band since: 1) unlike the 3.3 and $11.2\,\mu\text{m}$ bands, it could be observed by all three spectrometers on board ISO; 2) it is situated well outside the silicate absorption band and is the least influenced by extinction and 3) unlike the $7.7\,\mu\text{m}$ feature, it cannot be confused with a NGC 4418-like absorbed-continuum peak (Spoon et al. 2001, 2002). A clear line of sight towards AGN-heated hot dust may be recognized by the strong $6.2\,\mu\text{m}$ continuum associated with a hot dust power law spectrum. Since hot dust predominantly radiates at MIR wavelengths, the ratio of $6.2\,\mu\text{m}$ continuum over FIR flux will be high, far higher than for both star forming regions and AGNs without a clear line of sight to the AGN-heated hot dust. We therefore normalize our star formation indicator and our AGN hot dust indicator on the FIR flux (referred to as $6.2\text{PAH}/\text{FIR}$ and $6.2\text{cont}/\text{FIR}$). A clear disadvantage of this diagnostic is the often different apertures of the MIR and FIR instruments.

The continuum is estimated by drawing a polynomial of order 2 (i.e. straight line) through points at ~ 5.9 and $\sim 6.6\,\mu\text{m}$. Integrating the flux underneath it and above it in the range from 6.0 to $6.5\,\mu\text{m}$ gives respectively the strength of the hot continuum and the strength of the $6.2\,\mu\text{m}$ PAH feature. If a source exhibit water ice absorption (see Table 1 for Galactic sources and Spoon et al. (2002) for the galaxies), a local spline continuum is determined along the wing of the water ice band to estimate the $6.2\,\mu\text{m}$ PAH flux for Galactic sources while for extragalactic sources the $6.2\,\mu\text{m}$ PAH flux is recovered by defining a continuum at the base of the $6.2\,\mu\text{m}$ PAH feature. In order to obtain continuum strength corrected for ice extinction, the $6\,\mu\text{m}$ continuum strength is estimated by integrating a spline fixed just outside the ice absorption feature for these Galactic sources and by integrating the model continua derived in Spoon et al. (2002) for galaxies. The spectra of some galaxies show no evidence for $6.2\,\mu\text{m}$ PAH emission. For these galaxies, upper limits for the $6.2\,\mu\text{m}$ PAH flux are obtained by integrating a Gaussian with a peak flux of three times the rms noise and a FWHM of $0.185\,\mu\text{m}$.

For most galaxies, the FIR flux is computed from the 60 and $100\,\mu\text{m}$ IRAS Faint Source

Catalog (FSC) fluxes, applying the formula for $F(40\text{--}500\ \mu\text{m})$ as given in Sanders & Mirabel (1996). We assumed the correction factor C equaling 1.0 for $\text{IRAS60}/100 > 1.0$ and linearly increasing to 1.6 for $\text{IRAS60}/100 = 0.3$. The linear part of the correction factor is based on the galaxies Mrk1116, NGC3583, NGC4194 and NGC6090, for which we were able to perform a direct integration of the FIR SED. For galaxies with redshifts in excess of $z=0.1$, the FSC fluxes are a progressively worse probe of the rest frame 60 and $100\ \mu\text{m}$ fluxes. For these galaxies and galaxies lacking a $100\ \mu\text{m}$ FSC detection, we have supplemented the FIR SED with literature data and determined $F(40\text{--}500\ \mu\text{m})$ by direct integration of the obtained $40\text{--}500\ \mu\text{m}$ rest frame SED. For those galaxies for which additional FIR and submm literature data are not available, we looked for an observed SED that best matches the $5\text{--}60\ \mu\text{m}$ spectral properties and used its FIR and submm data beyond $60\ \mu\text{m}$ to compute the $F(40\text{--}500\ \mu\text{m})$ by direct integration of the $40\text{--}500\ \mu\text{m}$ rest frame SED. If no reliable match was found, we completed the SED with both a warm observed SED (e.g. 05189-2424) and a cold observed SED (e.g. IRAS19458+0944), resulting in two bracketing FIR fluxes. For QSOs we also considered power laws to provide the upper limits to the FIR flux. As pointed out in Sect. 3.2, ISO beams probe smaller physical scales than the IRAS beam. This mismatch becomes an issue when relating MIR to FIR fluxes for nearby galaxies for which the IR luminous regions do not completely fit within the smaller of the two apertures. We therefore screened our sample against spectra showing clear mismatches between the IRAS $12\ \mu\text{m}$ flux and the ISO $11\text{--}12\ \mu\text{m}$ continuum flux. Our sample should thus only consist of galaxies whose MIR emitting region fits entirely within the ISO aperture. For the FIR flux we will assume that it is dominated by the same (circum)nuclear star forming regions which give rise to the MIR continuum. Subsequently, the sample is screened against any spectrum for which the $6.0\text{--}6.5\ \mu\text{m}$ continuum is so noisy that the integrated $6.2\ \mu\text{m}$ flux would have to be replaced by an upper limit. Our final galaxy sample consists of 69 AGNs (7 QSO, 31 Sf1s and 31 Sf2s), 22 starburst and H II -type galaxies, 8 normal galaxies, 49 ULIRGs, 2 HyLIRGs and 3 IR galaxies with deeply obscured nuclei.

For the compact H II regions, the FIR flux is derived by fitting a modified blackbody to the IRAS PSC fluxes (Peeters et al. 2002b). However, ISO-SWS and IRAS have different beams ($20''$ versus $90''$). This may seriously affect the derived ratio of the MIR/FIR ratios if the source shows structure on a scale larger than the SWS beam. Therefore, we derive a scaling factor by matching the observed LWS flux to the SWS flux at $45\ \mu\text{m}$. Since the IRAS PSC fluxes – used to derive FIR fluxes – nicely correspond to the flux seen by ISO-LWS in the IRAS bands at 60 and $100\ \mu\text{m}$ for most sources (Peeters et al. 2002b), this scaling factor is a good correction. The derived FIR flux may still be incorrect for extended and complex sources. Since they nevertheless fit in with the overall envelope, we do show them in Fig. 4 in grey and indicate them in Table 1. For the extended molecular cloud M17–North,

30Dor and the RN NGC 7023, we integrated the LWS flux (45–200 μm) and scaled it with the above defined scaling factor. For a few sources, higher spatial resolution data (e.g. KAO with a beam of 35–60'') exist and we have used those to derive a FIR flux. M17 IRAM pos. 1 and 8 correspond to positions I and II in Meixner et al. (1992) and hence their FIR flux is derived from the incident UV flux, G_0 given by these authors and corrected for the beam difference. The FIR flux for Orion (MSX) and NGC7538 IRS1 is the FIR flux obtained with KAO observations, corrected for the difference in the beams. The ISO-SWS position in NGC2023 is closest to position H4 of Steiman-Cameron et al. (1997). We obtained its FIR from the FIR given for position P4 scaled by the ratio of the 64 μm continuum flux of position H4 to P4 (Steiman-Cameron et al. 1997). The FIR of ρ Oph, SMC B#1, DISM 1,2,3 and Milky Way (average) is estimated from their 100 μm continuum fluxes (135 μm continuum flux for SMC B#1) assuming a similar SED as that of cirrus (Boulanger et al. 1998a). We estimated the FIR for the central region of NGC891 from the observed UIR flux (in this central region) and the UIR/FIR ratio for the whole galaxy (Mattila et al. 1999). For the Orion Bar the FIR is taken from Werner et al. (1976).

The derived fluxes and the FIR references for the Galactic sample and the extragalactic sample are given in, respectively, Table 1 and Spoon et al. (in prep.).

4.1.1. *H II regions and ISM*

As discussed in Sect. 3.1, the 6.2PAH/FIR and the 6.2cont/FIR vary clearly within our sample of H II regions and this sequence extends up to the RNe and the (diffuse) ISM lines of sight (Fig. 4). Most sources are well localized in this diagram and are positioned along a strip going from the lower left towards the upper right, further referred to as the ‘fundamental line’. A clear segregation is present with embedded compact H II regions situated on the lower left side, while the RNe and the (diffuse) ISM are on the top right side. In addition, situated in the middle-right are the exposed PDRs, such as M17 (with pointings to the H II region, M17–1, and the molecular clouds, M17–8 and M17–North) and Orion. This segregation with object type suggests that the underlying cause may be a variation in the physical/chemical properties of the PAHs going from compact H II regions to exposed PDRs and the diffuse ISM, e.g. with G_0/n_e (Bakes et al. 2001a,b). Whether the segregation within the sample of H II regions is dominated by an evolutionary sequence — from ultra-compact to compact and then classical H II regions — is less clear. The 6.2PAH/FIR ratio correlates weakly with both the electron density and the size of the H II region (taken from Martín-Hernández et al. 2002, 2003). In contrast, the 6.2cont/FIR does not show a clear dependence on either the electron density or the size of the H II region. The latter also show large scatter

in Fig. 4, where many H II regions lie above the fundamental line. Likely, this reflects the contribution of hot dust inside the H II region. We note that metallicity does not seem to influence the location in this diagram. In particular, the SMC B1#1 and 30 Dor — with metallicities 0.3 and 0.1 of solar — lie close to their Galactic counterparts.

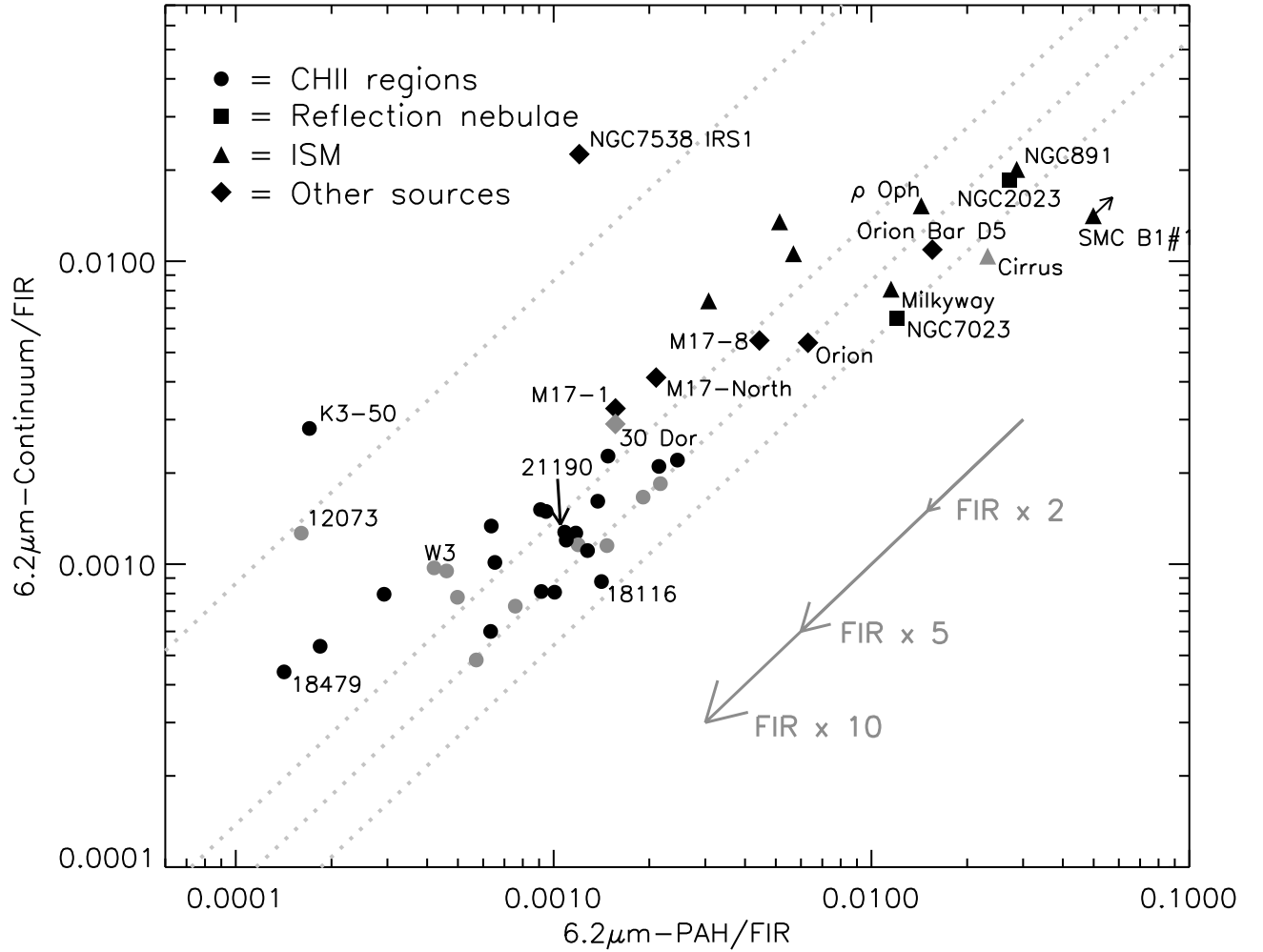


Fig. 4.— A MIR/FIR diagnostic diagram for the Galactic sample. The influence of an uncertain FIR flux is indicated by the arrows for respectively a factor of 2, 5 and 10. The *dotted lines* correspond to a $6.2\text{PAH}/6.2\text{cont}$ ratio of 0.116, 0.72, 1.16 and 1.85 from top to bottom. The sources possibly suffering from aperture effects are plotted in *grey*.

To guide the eye, we have drawn lines of constant 6.2PAH/6.2cont in Fig. 4. This ratio varies within the sample, ranging from 0.06 to 3.5 with an average of 1.0 ± 0.6 (0.93 ± 0.47 for only the H II regions). There seems to be a systematic trend: H II regions tend to lie above the bottom two lines while RNe and the diffuse ISM tend to lie between the bottom two lines. Three notable outliers are the Orion Bar, IRAS 12073 and K3–50A. The Orion Bar is located with the RNe suggesting a PDR dominated spectrum (cf. Tielens et al. 1993). IRAS 12073 has the lowest 6.2PAH/6.2cont ratio of the H II regions due to its very strong hot dust continuum. Indeed, IRAS 12073 is also the source with the largest Lyman continuum luminosity amongst the H II regions. As already pointed out, K3–50A has all the characteristics of H II regions except for its continuum which is more like that of massive protostars (see Sect. 3.1) and therefore likely has a similar 6.2PAH/6.2cont ratio as the highly embedded, pre-main-sequence object NGC 7538 IRS1 but shows the 6.2PAH/FIR characteristics of compact H II regions.

Based upon a comparison of H I recombination line fluxes and radio free-free fluxes, extinction in the MIR should be negligible for our sample of H II regions with $\tau_{\text{dust}}(6.2) \leq 1$ (Martín-Hernández et al. 2002, 2003, an A_K of 2 would decrease the 6.2PAH/FIR and 6.2cont/FIR with $\sim 20\%$). Hence, we conclude that the presence of a range in the 6.2PAH/FIR and 6.2cont/FIR ratios is real and that the sequence spanned by our sample likely reflects an “evolution” with object type : from embedded compact H II regions towards exposed PDRs and (diffuse) ISM.

4.1.2. *The galaxies*

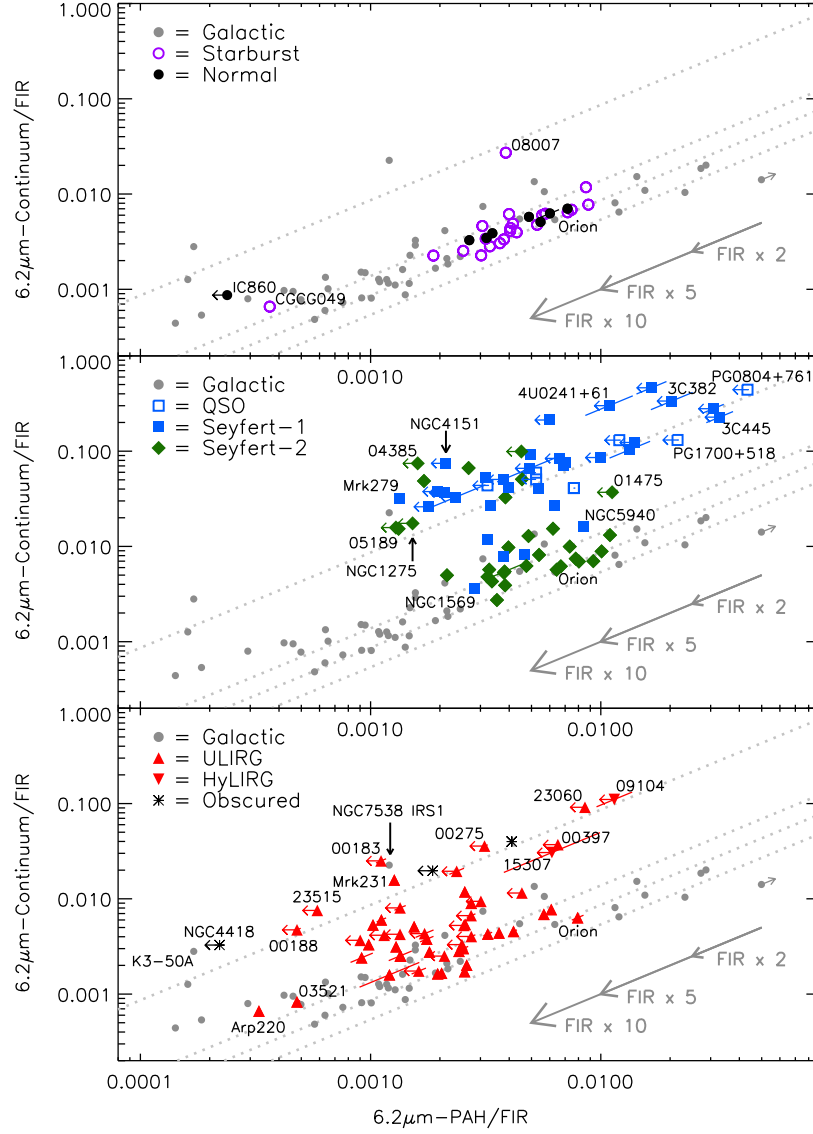


Fig. 5.— MIR/FIR diagnostic diagram for different type of galaxies. Grey circles correspond to Galactic sources. The three parallel *dotted lines* and the arrows are as in Fig. 4.

The normal galaxies occupy a narrow strip close to the position of the exposed PDR Orion (top panel, Fig. 5). Note the extreme position of IC 860, also found by Lu et al. (2003). ISO–LWS observations have revealed this source to be very unusual in not showing any of the typical FIR fine structure lines (Malhotra et al. 2001). Also the ISO–PHT–S spectrum is unusual, as it does not show $6.2\,\mu\text{m}$ PAH emission (see also e.g. Lu et al. 2003). The quality of the spectrum is, however, not good enough to speculate on the nature of the MIR spectrum.

Most starburst galaxies are found close to the position of the normal galaxies (top panel, Fig. 5), with the exception of IRAS 08007–6600 and CGCG 049–057. The ISO–PHT–S spectrum of IRAS 08007–6600 (classified by Veilleux & Osterbrock (1987) as H II -type) looks very similar to AGN hot dust dominated spectra and was therefore classified by Laureijs et al. (2000) as AGN-dominated. The spectrum of CGCG 049–057 is PAH-dominated, but has a very strong and cold FIR continuum. Note that the starburst galaxies (excluding the latter two) occupy a larger range along the fundamental line than normal galaxies do, and look, on average, like exposed PDRs with similar $6.2\text{PAH}/6.2\text{cont}$ ratios.

The distribution of AGNs seems to segregate into two groups (middle panel, Fig. 5). One group (group A) is made up mostly of Sf2s with IRAS S 25/S 60 ratios all below 0.25, while the other group (group B) consists mostly of Sf1s and QSOs with IRAS S 25/S 60 ratios all larger than 0.25. The galaxies in group A all show $6.2\text{PAH}/\text{FIR}$ ratios in the same range as normal and starburst galaxies. In contrast, most of the galaxies in group B only have formal $6.2\text{PAH}/\text{FIR}$ upper limits, some of which are found at $6.2\text{PAH}/\text{FIR}$ ratios 2–3 times larger than the highest value found for normal and starburst galaxies. These upper limits shift left and fit in with the rest of their group (B) if the scaling by FIR flux is replaced by a scaling by the total IR flux ($8\text{--}1000\,\mu\text{m}$; Sanders & Mirabel 1996). In line with the orientation dependent unification scheme (Antonucci 1993), the segregation in $6.2\text{cont}/\text{FIR}$ between the two groups likely reflects the orientation of the toroid structure around the nucleus which for the lower group (A) may block our line of sight to the warm inner toroid, responsible for the $6\,\mu\text{m}$ continuum. Assuming this to be the case, a separation of a factor 10 in $6.2\text{cont}/\text{FIR}$ may be interpreted as an $A(V)=50\text{--}150$ (depending on the choice of extinction law), which (assuming a normal gas to dust ratio $N_H=1.9\times 10^{21}\text{ A}_V$) is equivalent to a column density of $10^{23.0}\text{--}10^{23.5}\text{ cm}^{-2}$. This range is in good agreement with the mean Sf2 absorbing column, as measured directly from X-ray data (Risaliti et al. 2002), and with the results of Clavel et al. (2000). The presence of some Sf1s in groups A (NGC 1569, Mrk 789, NGC 5940 and NGC 7469) would then imply that the intrinsic power of the AGN in these galaxies must be small for the AGN hot continuum not to dominate the MIR spectral appearance. Alternatively, the AGN hot continuum and the optical AGN diagnostic lines emanating from these galaxies are obscured by patchy foreground dust clouds along the line of sight in the

host galaxy, but still allowing an optical classification. Conversely, the presence of some Sf2s in group B (NGC 1068, NGC 1275, Mrk 463, IRAS 04385–0828, NGC 5506 and PKS 2048–57) would then be explained by a direct line of sight, at grazing angle, to the inner edge of the torus, or by the presence of dust clouds above the plane of the torus, which are irradiated and heated by the central source or a more powerful AGN.

One of the key predictions of the unification scheme is that the properties of the Seyfert host galaxies are independent of the orientation of the torus and, hence, independent of Seyfert type. Clavel et al. (2000) have tested this with the $7.7\ \mu\text{m}$ PAH luminosity distributions for Sf1s and Sf2s and found that they were the same for their sample. We have repeated this test for our sample of Seyfert galaxies (43 Sf1s; 51 Sf2s). The resulting luminosity distributions are shown in Fig. 6. If upper limits are counted as detections, both Seyfert types have the same median $6.2\ \mu\text{m}$ PAH luminosity of $10^{8.1}\text{ L}_{\odot}$. If upper limits are excluded, the median values are still very similar, $10^{8.2}\text{ L}_{\odot}$ for Sf1s and $10^{8.3}\text{ L}_{\odot}$ for Sf2s. Our results are therefore consistent with those of Clavel et al. (2000).

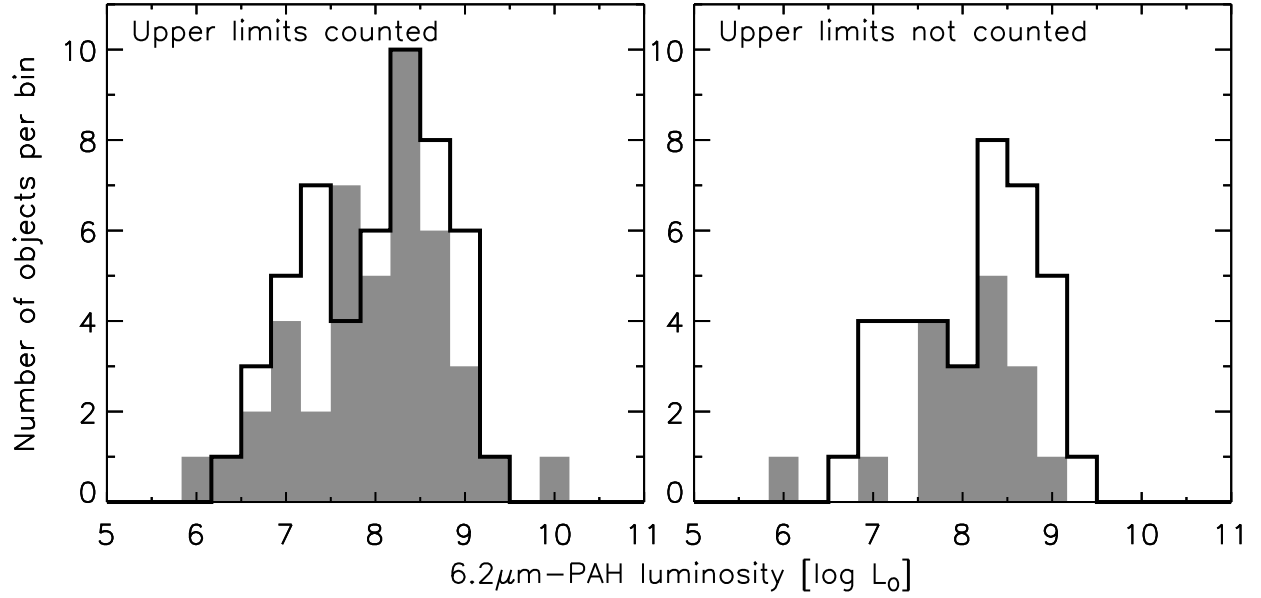


Fig. 6.— Luminosity distribution of the 6.2 μm PAH feature for Sf1s (*filled grey*) and Sf2s (*black*). The bin sizes are 0.33 dex. **Left panel:** Upper limits on the PAH flux are counted as detections. **Right panel:** Upper limits on the PAH flux are excluded.

Even more dusty are the nuclei of most ultra-luminous IR galaxies. ULIRGs, HyLIRGs and galaxies with deeply obscured nuclei cover a large portion of the diagram, reflecting their wide-ranging properties (lower panel, Fig. 5). Galaxies in the upper right section (e.g. I00397–1312, I00275–2859, I09104+4109, I15307+3252 and I23060+0505), all have IRAS S25/S60 ratios and MIR spectra similar to AGNs in that same section and are likely AGN-dominated. In contrast, some ULIRGs show spectra similar to Orion and other bonafide star formation regions and are likely dominated by star formation. Many other ULIRGs occupy a space not covered by any other (extra)galactic source and are situated to the left of both Seyfert distributions. The nuclei of these ULIRGs are therefore evolving from completely embedded to less obscured nuclei. Notable outliers are Arp 220 and I03521+0028, which are found among the CH II regions, close to the position of another outlier, IC 860. Since the spectrum of Arp 220 is deficient in emission lines (Spoon et al. 2004) – characteristic of CH II regions – this source is likely shifted down from the ULIRG domain, due to the presence of an additional strong FIR component, which is not commonly present in other ULIRGs (Spoon et al. 2004). Given their close proximity to Arp 220, I03521+0028 and IC 860 may also harbor similar FIR bright components.

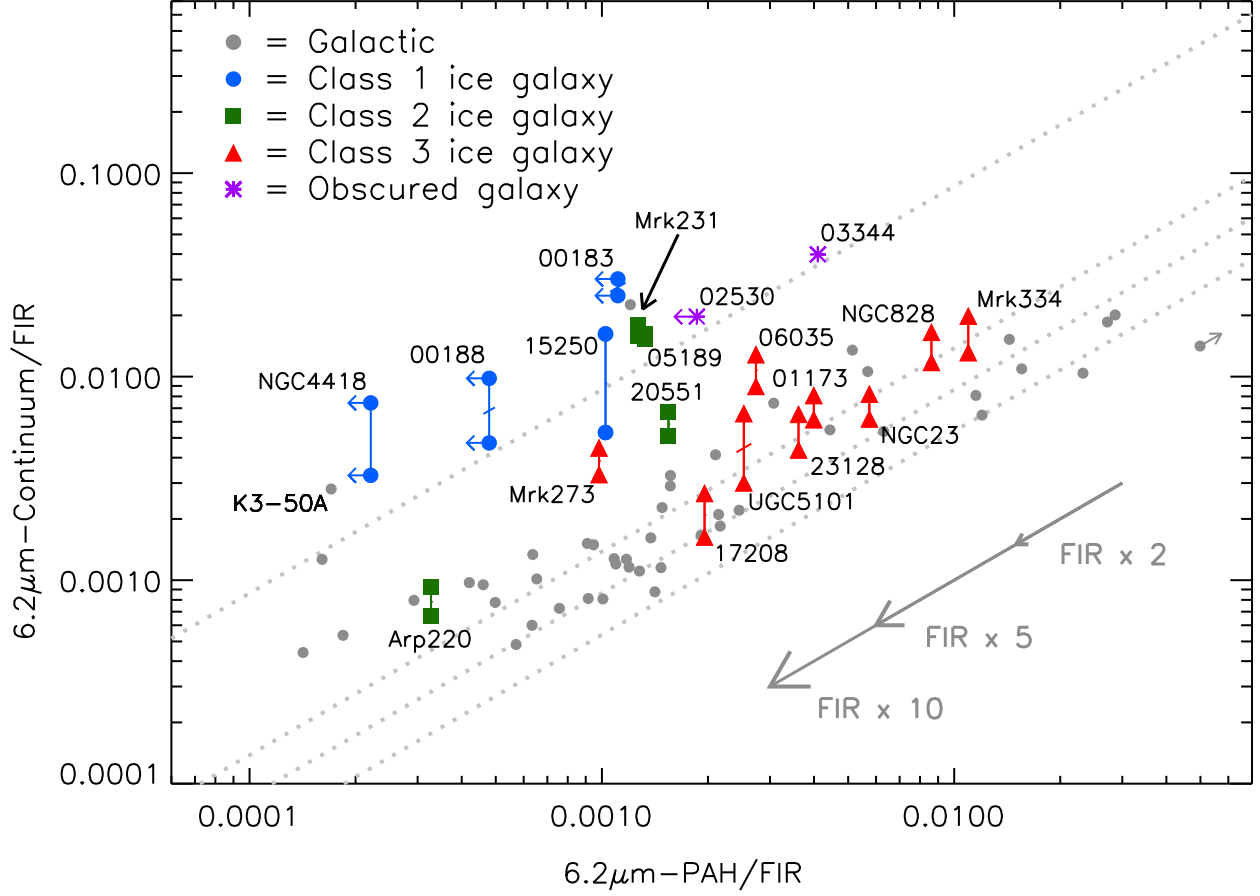


Fig. 7.— MIR/FIR diagnostic diagram for deeply obscured galaxies and ice galaxies. The *dotted lines* and the *arrows* are as in Fig. 4. A vertical *line* indicates the upward shift of an ice galaxy if the measured $6.2\mu\text{m}$ continuum is corrected for the presence of $6.0\mu\text{m}$ water ice absorption.

Fig. 7 shows the distribution of a subset of galaxies in which the $6.0\,\mu\text{m}$ water ice feature has been identified (Spoon et al. 2002), the so-called ‘ice galaxies’. The sample has been appended with I03344–2103 and I02530+0211, which show similarly deep silicate absorption features as the class 1 and class 2 ice galaxies. However, shortward of the silicate feature both spectra show features which are likely artifacts. For I02530+0211 it is nevertheless clear that the $5.8\text{--}6.5\,\mu\text{m}$ spectrum is feature-free and for I03344–2103 the presence of weak $6.2\,\mu\text{m}$ PAH emission can be confirmed; the presence of a $6.0\,\mu\text{m}$ water ice absorption feature, however, cannot be confirmed.

Generally, ice extinction is weak and has little influence on these ratios. However, assuming that the PAH emission arises from a circumnuclear region which is unaffected by extinction, strong ice band sources would shift up by a factor of 2–3 (Spoon et al. 2002).

Class 3 ice galaxies, showing weak $6.0\,\mu\text{m}$ ice band absorptions, coincide with the location of the normal and starburst galaxies in this diagram. Compared to class 3, class 1 ice galaxies, with no obvious PAH features and strong $6.0\,\mu\text{m}$ ice and silicate bands are shifted upwards and to the left in Fig. 7, betraying the addition of extra MIR continuum as well as FIR continuum. In particular, we note that the extreme example of this class, NGC 4418, is located close to K3-50 A. The few class 2 ice galaxies, with weak PAHs and moderate ice absorptions, are more scattered throughout this plot. Some (I20551–4250) fall in between the two other classes. Others coincide with class 1 (Mrk 231 and I05189–2524). Arp 220, which has weak ice absorption, has shifted downwards along the Galactic trend and is an outlier in this diagram (see above). It is clear that the absorption associated with molecular clouds can influence the location of a region in this diagram.

In Spoon et al. (2002), we proposed that the classification of ice galaxy spectra may reflect an evolutionary sequence from strongly obscured beginnings of star formation (and AGN activity) to a less enshrouded stage of advanced star formation (and AGN activity). Assuming NGC 4418 to represent the earliest, most obscured stage after a galaxy collision or merger, evolution would then proceed towards the lower distribution for galaxies which in the MIR are dominated by star formation (and may contain a Sf2 nucleus), or towards the upper distribution for galaxies which in the MIR are AGN-dominated.

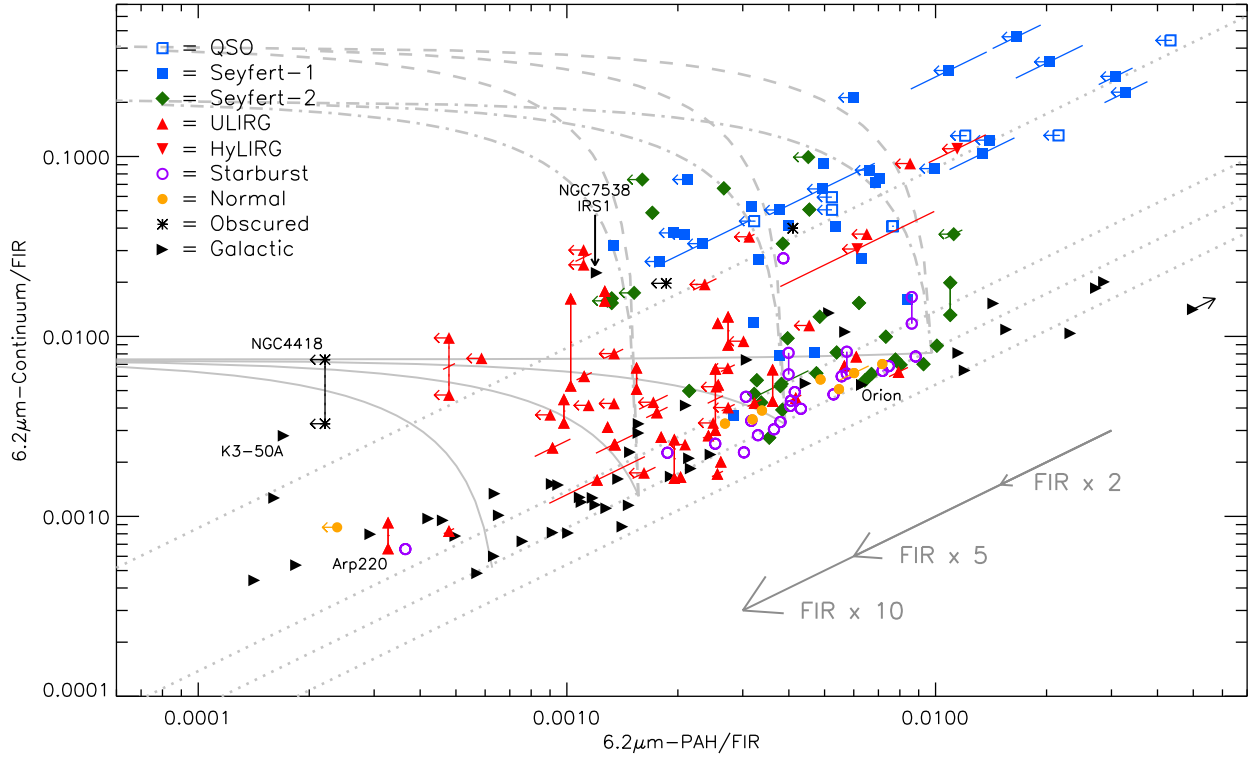


Fig. 8.— The MIR/FIR diagnostic diagram for all sources. The *dotted lines* and the *arrows* are as in Fig. 4. The *continuous lines* are mixing lines between heavily obscured and exposed star formation. The mixing lines from starburst- to AGN-dominated MIR spectra are represented by the *dashed* and *dot-dashed lines*, assuming respectively 25% and 50% of the FIR flux to be associated with AGN hot dust. See text for details.

4.1.3. Application of diagnostic

MIR galaxy spectra can show the spectral characteristics of star forming regions, AGN-heated dust and/or obscuration (Sect. 3.2). As pointed out above, spectra of clear lines of sight to AGN-heated dust are located in other parts of the MIR/FIR diagnostic diagram than spectra for which this line of sight is blocked by the AGN torus and which are therefore PAH-dominated. In order to better understand the connection between these two groups we have calculated the diagnostic ratios that result from adding AGN hot dust spectra to several choices of PAH-dominated spectra. For a pure AGN-heated dust template, we used the nuclear spectrum of the prototypical Sf1, NGC 4151, and set its 6.2PAH/FIR ratio equal to 0. As the FIR flux associated with AGN hot dust has not been directly measured for NGC 4151 (nor for any other galaxy), we determine two values for its 6.2cont/FIR ratio, assuming 25% and 50% of the FIR flux to be associated with the AGN hot dust. For the starburst template, we choose the central region of the starburst galaxy M 83. Other PAH dominated galaxy spectra along the fundamental line are then mimicked by scaling its FIR flux up and down by a factor 3. Dashed and dash-dotted lines in Fig. 8 represent the calculated mixing lines, further referred to as ‘AGN-starburst’ tracks. The tracks strikingly illustrate the direction in which a Seyfert galaxy spectrum moves if the orientation of the AGN torus changed in order to have less obscuring dust in the line of sight to the hot inner wall of the torus. Alternatively, they illustrate the effect of an increase in AGN power. The absence of Seyfert galaxies along the horizontal part of these tracks is due to a combination of ISO’s inability of detecting the ‘weak’ PAH emission on such strong continua and the non-negligible contribution of star formation from the host galaxy.

Similarly, starburst and heavily obscured galaxies are found in far-apart regions in the MIR/FIR diagnostic diagram. We illustrate the connection between these two groups by calculating the diagnostic ratios that result from adding PAH dominated spectra to that of an heavily obscured nucleus (NGC 4418). In this way, we mimic the degree of obscuration. We further used the same starburst templates as for the AGN-starburst tracks, but added another fundamental line ‘starting’ point in the lower left quadrant, by scaling the FIR flux of M 83 up by a factor 30. These tracks – further referred to as ‘obscured-starburst’ tracks – are shown by solid lines in Fig. 8. Note that H II regions located above the fundamental line do not necessarily suffer from obscuration (Sect. 4.1.1).

A third set of mixing lines connects heavily obscured nuclei (e.g. NGC 4418) and galaxies dominated by AGN hot dust (e.g. NGC 4151). Assuming no PAH emission from either type of source (as for the other mixing lines) implies these tracks would run vertical. Taking into account a contribution of star formation to the spectra of Seyferts will cause these tracks to run almost parallel to the lines of constant 6.2PAH/6.2cont ratio. As several ULIRGs with

signs of strong obscuration (i.e. I00183–7111, Mrk231 and I00275–2859) are lined up along these mixing lines, these three ULIRGs may well harbour a hidden AGN.

No galaxies are found with 6.2PAH/FIR ratios below 0.002–0.003 on the main sequence (Fig. 8). Assuming this to be the lowest attainable 6.2PAH/FIR value for pure starburst or normal galaxies, our tracks suggest that galaxies found at $6.2\text{PAH}/\text{FIR} < 0.002$ likely contain an obscured nuclear component. Interestingly, this would then indicate that a large fraction of the ULIRG nuclei is obscured.

Note that our simple mixing model does not offer an explanation for the extreme positions of Arp 220, IC 860, CGCG 049–057 and I03521+0028, found in the lower left quadrant of the diagram.

4.2. Laurent diagnostic diagram

Another diagnostic solely based on the MIR spectrum is proposed by Laurent et al. (2000). These authors assume that the MIR emission of galaxies originates in 1) AGN-heated dust, characterized by a strong dust continuum shortwards of $10\ \mu\text{m}$, 2) PDRs, characterized by PAH emission, and 3) H II regions, characterized by strong dust continuum longwards of $10\ \mu\text{m}$. To quantify their relative contributions, two diagnostic indicators are used, the ratio of warm (14–15 μm) to hot (5.1–6.8 μm) dust continuum and the ratio of 6.2 μm PAH emission to hot dust continuum. Note that the latter indicator is similar to the offset ($6.2\text{PAH}/6.2\text{cont}$) of a source from the fundamental line in the MIR/FIR diagnostic.

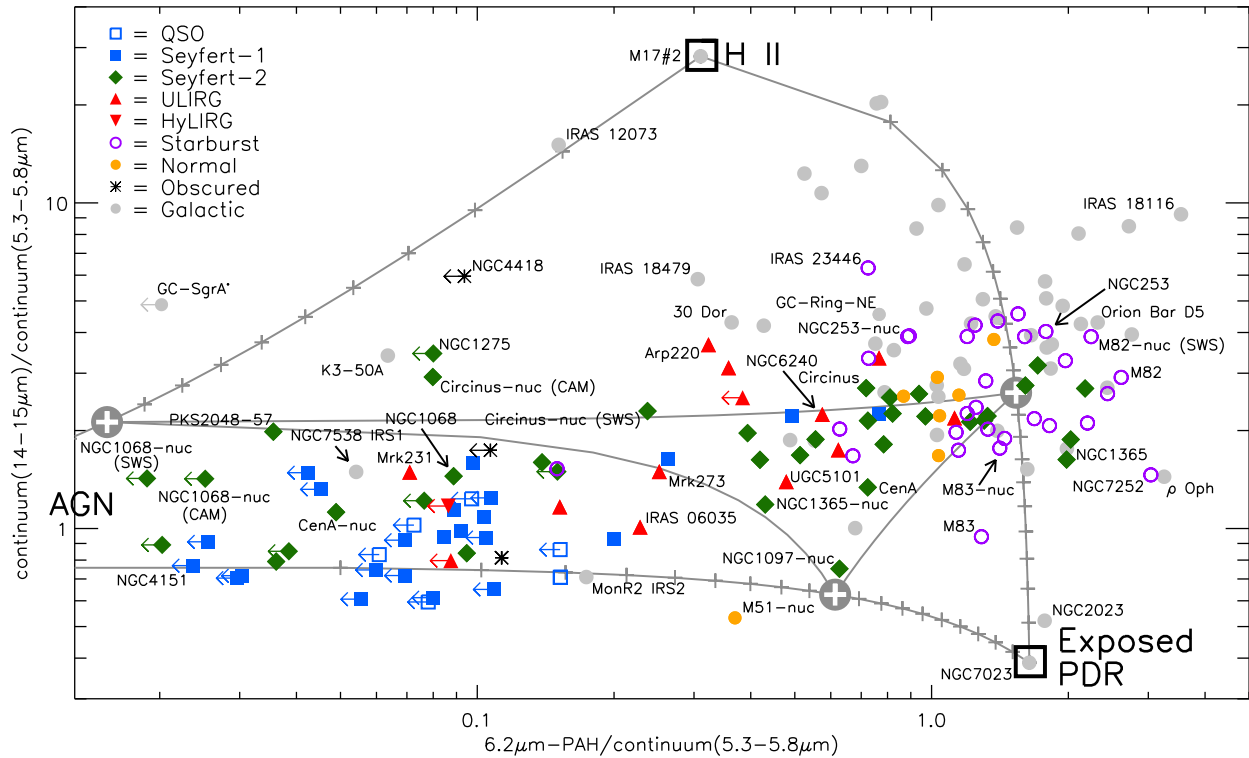


Fig. 9.— MIR diagnostic diagram adapted from Laurent et al. (2000). The three templates are indicated by their name (PDR, HII or AGN) and a large open square. Since the AGN template has per definition no PAH flux, it falls off the plotted x-range (at the left). The *grey lines* connecting the three templates are mixing lines between the templates. Each *grey cross* indicates a 5% change in relative contribution. *Thick crosses* mark equal contribution of two templates. The *grey lines* connecting the three *thick crosses* indicate a constant 50% fraction of one component along each line. The SMC source B1#1 is located off the diagram at position (3.0,0.16).

We choose to sample the hot continuum at shorter wavelengths (i.e. $5.3\text{--}5.8\,\mu\text{m}$; referred to as 5.5cont) than Laurent et al. (2000), in order to be a) more sensitive to the slope between hot and warm continuum and b) to avoid sampling within the $6.0\,\mu\text{m}$ ice absorption band. For the warm continuum we adopt the same integration range as Laurent et al. (2000): $14.0\text{--}15.0\,\mu\text{m}$, referred to as 15cont. The $6.2\,\mu\text{m}$ PAH flux is determined as defined in Sect. 4.1. The derived fluxes for the Galactic sample and the extragalactic sample are given in, respectively, Table 1 and Spoon et al. (in prep.).

The selection criteria for this diagram are somewhat different than for the previous diagram (Sect. 4.1), as not all galaxy spectra are available over the full $5.3\text{--}15.0\,\mu\text{m}$ range. ISO–PHT–S spectra, for instance, only cover the ranges $2.47\text{--}4.77\,\mu\text{m}$ and $5.84\text{--}11.62\,\mu\text{m}$. For targets at low redshift this means that the 5.5cont cannot be measured directly. We therefore performed a linear interpolation over the $4.77\text{--}5.84\,\mu\text{m}$ gap for those spectra which have sufficient S/N on both sides. Targets which did not meet this criterion, mostly ULIRGs, were eliminated from the sample. For sources with redshifts $z > 0.1$ the gap in the ISO–PHT–S spectral coverage is not an issue. ISO–PHT–S spectra also present a problem at the long wavelength end, as their wavelength coverage ends at $11.62\,\mu\text{m}$. In order to derive a 15cont for these cases, we logarithmically interpolated the IRAS $12\,\mu\text{m}$ and $25\,\mu\text{m}$ fluxes to the $14\text{--}15\,\mu\text{m}$ range. However, sources were removed from the sample if their IRAS $12\,\mu\text{m}$ fluxes are upper limits, or if there is a clear mismatch between the ISO–PHT–S spectrum and the IRAS $12\,\mu\text{m}$ flux. While the former criterion results in the exclusion of many fainter ULIRG spectra, the latter criterion results in the non-selection of many nearby galaxies. We then screened against sources with $5.3\text{--}5.8\,\mu\text{m}$ spectra which are either too noisy or which show artifacts, as is the case for several ISO–CAM–CVF spectra. Our final galaxy sample consists of 66 AGNs (6 QSOs, 23 Sf1s and 37 Sf2s), 30 starburst and H II -type galaxies, 7 normal galaxies, 13 ULIRGs, one HyLIRG and 3 IR galaxies with deeply obscured nuclei. Note that some galaxies are close enough for ISO to obtain spectra of both the central region and the entire ISO–CAM–CVF field of view. These galaxies are NGC 253, NGC 1068, NGC 1365, NGC 1808, Cen A, Circinus and M 83.

4.2.1. *H II regions and ISM*

The H II regions do not form a narrow sequence in this diagram but show a wide spread scattering over about 1/3 of the plot. However, they do avoid the low PAH and low warm continuum properties of the AGNs. Correcting for extinction (for sources with known A_K) does not reduce the observed spread. However, it clearly has some influence on the precise position of the sources; an A_K of 2, which is typical for these H II regions (Martín-

Hernández et al. 2002, 2003), gives rise to an increase of 7% and 15% in $6.2\text{PAH}/5.5\text{cont}$ and $15\text{cont}/5.5\text{cont}$, respectively. The Orion Bar is now positioned with the H II regions instead of with the RNe (Sect. 4.1.1). Obviously, Galactic sources offset from the fundamental line in the MIR/FIR diagram (i.e. with unusual $6.2\text{PAH}/6.2\text{cont}$ ratios) are also outliers in this diagram (i.e. at unusual $6.2\text{PAH}/5.5\text{cont}$ ratios) but are easier notable here. Hence, similar conclusion can be drawn as for the MIR/FIR diagnostic. Highly embedded regions (NGC7538 IRS1, Mon R2 IRS2, and K3–50A) are found at low $6.2\text{PAH}/5.5\text{cont}$ and low $15\text{cont}/5.5\text{cont}$, clearly away from H II regions and much closer to the AGN template.

4.2.2. Galaxies

The majority of galaxies are found in a wide strip, almost horizontally (within a factor of 3) across the diagram (Fig. 9). This sequence runs from normal and starburst galaxies on the right (coinciding with the H II regions), through the ULIRGs in the middle to the Sf1s on the left. Sf2s are predominantly located on the right, but are found along the full range, depending on the degree of dilution of the AGN hot dust continuum by a PAH dominated spectrum. This depends on both the physical size covered by the aperture and the fraction of the bolometric luminosity contributed by star formation. We note the close similarity between the MIR characteristics of the Orion Bar and the nucleus of starburst galaxy M82. In contrast, the spectrum of the entire M82 field-of-view is closer to that of RNe. The same trend is observed for M83. Apparently, galaxy disks are dominated by stellar types slightly more similar to RNe. Fig. 9 reveals small differences in continuum slope among AGN nuclei, for example between the nuclear spectra of NGC 1068 (Sf2) and NGC 4151 (Sf1). As pointed out by Laurent et al. (2000), the spectra of the AGN host galaxies are dramatically different from those of the AGN itself and resemble those of normal and starburst galaxies instead. A good example is the nearby Sf2 Cen A (Laurent et al. 2000). While its integrated galaxy spectrum is PAH dominated and is found among the starburst galaxies, the nuclear spectrum shows hardly any PAH emission and is situated with the AGNs. Unlike the MIR/FIR diagram, where ULIRGs occupy their own niche, ULIRGs are not separated out as much. Some ULIRGs (Mrk 231 and I 23060+0505) and the HyLIRG I 09104+4109 are found among the pure AGNs, while other ULIRGs, like I 17208–0014, are found among the starburst galaxies. The remaining ULIRGs are found more towards the center of the plot. The highly obscured source NGC 4418 has a ratio of $15\text{cont}/5.5\text{cont}$ which is very similar to that of the prototypical starburst galaxy M82. However, it lacks the strong $6.2\text{ }\mu\text{m}$ PAH feature of M82 and hence its $6.2\text{PAH}/5.5\text{cont}$ ratio is typical of pure AGN spectra; the slope of its continuum is however much steeper. Other sources with moderate to strong obscuration are found in the lower left quadrant, overlapping to some extent with the Galactic embedded star

forming regions (Fig 9). Note that Arp 220 is found in between NGC 4418 and the average position of starburst galaxies, in agreement with the results of Spoon et al. (2004).

4.2.3. *Application of diagnostic*

Similar to Laurent et al. (2000), we calculated mixing lines where the contribution of each template to the MIR flux (measured from 5.3 to 15 μm) varies between 0 and 100% (Fig. 9). The three templates used, are the spectra of NGC 7023 (exposed PDR), M 17 at position 2 (H II region) and NGC 4151 (AGN-heated dust). The templates are represented in Fig. 9 by large open squares except for the AGN template for which we assumed a PAH flux of zero instead of the derived upper limit. It is important to realize that the mixing percentages can only be interpreted as percentages of *MIR* and not *total* IR luminosity. This is especially true for the AGN contribution, as the same AGN may have a factor 10 higher or lower continuum flux, solely depending on the degree of obscuration towards the central source.

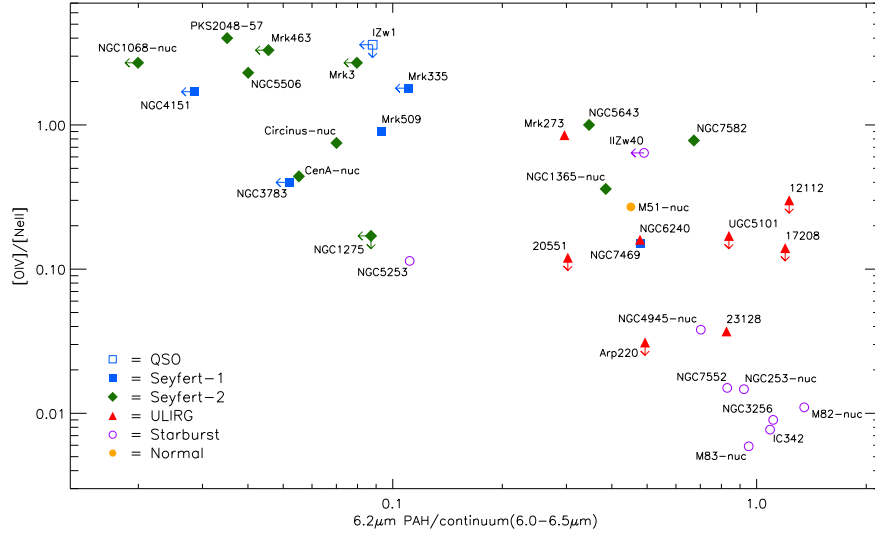


Fig. 10.— MIR diagnostic diagram for different type of galaxies, adapted from Genzel et al. (1998). AGN-dominated MIR spectra are found in the upper left quadrant, while starburst-dominated MIR spectra are found in the lower right quadrant.

Our sample of H II regions is clearly not just dominated by emission of hot dust from the H II region but also shows significant contribution from the surrounding PDR. The sequence from PDRs to H II regions is not well determined observationally. Using other templates to calculate the mixing lines would change its position. Indeed, this is forcefully brought home by the many objects which lie outside the mixing lines which span the diagram. Changing the templates will not remove the spread of the observed H II regions along a mixing line. Hence, H II regions can only be described in first order by a combination of an H II region and PDR template.

Embedded protostars are easily distinguished from H II regions and PDRs in this diagram by their lower $6.2\text{PAH}/5.5\text{cont}$ ratio. Unfortunately, their location coincides with that of AGN-dominated spectra. Hence, this diagnostic diagram cannot distinguish between MIR spectra dominated by an AGN or by a deeply embedded source. This is of particular interest for ULIRGs whose MIR spectra have the signature of star formation, AGN-heated dust or dust extinction (Sect. 3.2). With this diagram, only the first can be discerned from the rest.

The PAH contribution to the MIR spectrum of Seyferts is best traced by the $6.2\text{PAH}/5.5\text{cont}$ ratio, which is highly sensitive to small fractions of (exposed) PDR contribution included within the beam. These contributions usually arise from circumnuclear star formation rings or from the galaxy disk. Note that for starburst galaxies the inclusion of a larger part of the galaxy disk does not result in a similar strong shift as for Seyferts in either diagnostic ratio.

4.3. The Genzel diagnostic diagram

A MIR diagnostic diagram which also successfully separates Seyfert galaxies from starburst galaxies is the diagram proposed by Genzel et al. (1998). As seen in Sects. 4.1 and 4.2, the use of the $6.2\text{PAH}/6.2\text{cont}$ (or equivalently the $7.7\text{ }\mu\text{m}$ PAH line-to-continuum) is an excellent choice for determining the importance of star formation in the MIR. Likewise, the ratio of the high excitation fine-structure line $25.9\text{ }\mu\text{m}$ [O IV] to the low excitation fine-structure line $12.8\text{ }\mu\text{m}$ [Ne II] is a good tracer for AGN activity. Here we show a modified version of this diagram, in which we replaced the $7.7\text{ }\mu\text{m}$ PAH line-to-continuum ratio by the $6.2\text{PAH}/6.2\text{cont}$ (Fig. 10). We note that our Galactic sample does not exhibit the high excitation fine-structure line $25.9\text{ }\mu\text{m}$ [O IV] emission.

The number of galaxies in our Genzel diagram is limited by the availability of line fluxes of $12.81\text{ }\mu\text{m}$ [Ne II] and $25.9\text{ }\mu\text{m}$ [O IV] from the literature. For AGNs the line fluxes were taken from Sturm et al. (2002), for starburst galaxies from Verma et al. (2003) and for ULIRGs from Genzel et al. (1998). Our final sample consists of 17 AGNs (1 QSO, 5 Sfls,

11 Sf2s), 8 ULIRGs, 9 starburst galaxies and 1 normal galaxy.

The $[\text{O IV}]/[\text{Ne II}]$ ratio by itself is effective in separating Seyfert (both Sf1s and Sf2s) from starburst galaxies, as Seyferts have ratios higher than 0.1 and starburst galaxies have ratios lower than ~ 0.02 (Fig. 10). Exceptions are low metallicity galaxies, e.g. NGC 5253 and IIZw40. The other diagnostic ratio, $6.2\text{PAH}/6.2\text{cont}$, is not a reliable separator of Sf1s and Sf2s on one hand and starburst galaxies on the other hand. This was already discussed in the context of the MIR/FIR diagram and is strikingly illustrated in the Genzel diagram by the examples of the Seyferts NGC 7469 and NGC 7582, which appear starburst-like in their $6.2\text{PAH}/6.2\text{cont}$ ratios, but which are AGN-like in their $[\text{OIV}]/[\text{NeII}]$ ratios. Other Seyferts would show a similar disagreement in their diagnostic ratios, had their properties been represented by their integrated galaxy spectra instead of their nuclear spectra. Examples are Cen A and Circinus. Based on the above, we conclude that the $[\text{OIV}]/[\text{NeII}]$ ratio is a more reliable AGN indicator than the $6.2\text{PAH}/6.2\text{cont}$. Applying the $[\text{O IV}]/[\text{Ne II}]$ ratio to find AGNs in ULIRGs, only 2 out of 8 ULIRGs harbor an AGN (NGC6240 and Mrk 273). The other 6 ULIRGs either have upper limits or have a ratio intermediate to those typical for Seyferts and starbursts (I 23128–5919).

The nucleus of the nearby starburst galaxy NGC 4945 is found at an intermediate $[\text{O IV}]/[\text{Ne II}]$ ratio. The elevated $[\text{O IV}]/[\text{Ne II}]$ ratio for this source is likely due to strong differential extinction between $12.81\mu\text{m}$ and $25.9\mu\text{m}$ in this notoriously dusty nucleus (Spoon et al. 2000). Hard X-ray observations have shown this galaxy to contain a buried AGN (Iwasawa et al. 1993; Guainazzi et al. 2000), which so far has escaped detection at NIR and MIR wavelengths. Therefore, NGC 4945 may be taken as a warning that some AGNs may escape detection also from MIR excitation indicators like $[\text{O IV}]/[\text{Ne II}]$. Other highly obscured galactic nuclei, like NGC 4418 and Mrk 231, have not even been detected in $12.81\mu\text{m}$ $[\text{Ne II}]$ (Spoon et al. 2001; Genzel et al. 1998). For these galaxies, and likely also for many ULIRGs, the Genzel diagnostic diagram is not well suited.

4.4. Comparison of the three diagnostic diagrams

Each of the three diagnostic diagrams is constructed with the immediate goal to reveal the identity of a galaxy.

All three diagnostics are able to identify Sf1s. The degeneracy between starburst and Sf2s can only be broken by the Genzel diagram. Indeed, by using the $[\text{O IV}]/[\text{Ne II}]$ ratio, the Seyferts are clearly separated from the starburst galaxies. In contrast, starburst galaxies and Sf2s occupy the same region in the MIR/FIR and Laurent diagnostic diagram. This

illustrates that the identification of the dominant power source — AGN or starburst — highly depends on the wavelength region considered. Conversely, such an identification does not imply a similar degree of dominance in the *total* IR luminosity.

Heavily obscured galaxies are best recognized in the MIR/FIR diagram. Since they show no or lack detectable fine-structure lines, they are absent in the Genzel diagram, while in the Laurent diagram — which was also not constructed for these type of galaxies — they can be mistaken for AGN-dominated sources. Only the MIR/FIR diagram seems to be able to separate out ULIRGs showing signatures of obscured star formation or obscured AGN activity.

5. Discussion

5.1. PAH abundance

The ratio of the total PAH emission to the FIR emission measures the competition of the PAHs and the dust for the UV photons and is, thus, an indicator for the PAH/dust abundance. Studies of PAH/FIR ratios in Galactic sources have revealed that this ratio is independent of the local radiation field, G_0 , for low radiation fields and decreases with G_0 at higher radiation fields (Boulanger et al. 1998a,b; Onaka 2000). These authors suggested that this proportionality of PAH strength with G_0 for low G_0 (since PAH/FIR is constant with G_0) is consistent with emission coming from species small enough to be stochastically heated. The decrease for high G_0 is then taken to indicate a decreasing abundance of these species relative to that of the grains with increasing strength of the illuminating radiation field.

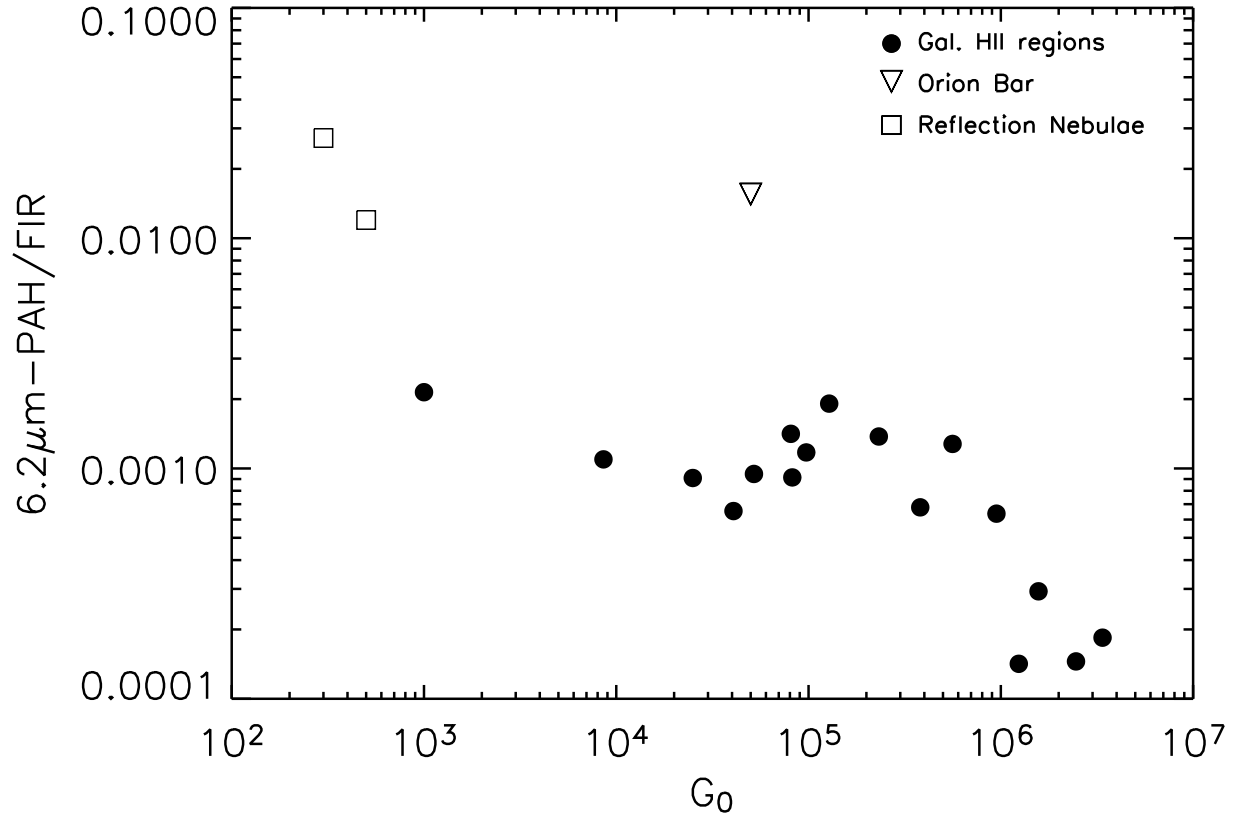


Fig. 11.— The relation of $6.2\text{PAH}/\text{FIR}$ with the local radiation field, G_0 for H II regions. As a reference, two RNe are also shown.

To first order, the PAH/FIR can be traced by the 6.2PAH/FIR since the fraction of total PAH flux emitted in the 6.2 μm PAH band varies only from 14 to 38 % with an average of $28 \pm 4\%$ (Vermeij et al. 2002; Peeters et al. 2002a). We derived G_0 values from the IR flux and the angular size of the PAH emission region (cf. Hony et al. 2001). This assumes that all the UV light is absorbed in a spherical shell with the angular diameter of the H II region and re-emitted in the IR. Since the PAHs are expected to be destroyed inside the H II region, it is reasonable to use the radio size of the H II regions (taken from Peeters et al. (2002b) and Martín-Hernández et al. (2003)). For G_0 values for the Orion bar and the RNe, we refer to Tielens et al. (1993), Joblin et al. (1996), and Hony et al. (2001). Extended and complex H II regions are excluded due to possible aperture effects.

Fig. 11 shows the relation between 6.2PAH/FIR and G_0 for our sample of H II regions. Taking into account the results of Boulanger et al. (1998a,b) for $G_0 < 10^3$, this relation seems to be a step function with steps at $G_0 \sim 10^3$ and $\sim 10^6$, exposing the Orion Bar as a clear outlier. Indeed, sources with similar 6.2PAH/FIR show a large spread in G_0 , up to a factor 10^3 . This first step was seen by Boulanger et al. (1998a,b) based on the difference between regions with low G_0 and the H II region M17. In contrast, Onaka (2000) found a loose correlation between 7.7PAH/FIR versus G_0 for different positions within the Carina Nebula (with only a factor up to 7 difference in G_0 for positions with similar 6.2PAH/FIR). The presence of such a relationship within a single object seems to be a more general characteristic of the PAH emission behavior. Apparently, within a single object, variations in G_0 are important in driving the emission spectrum. However, the source to source variation in the PAH/FIR ratio does not seem to follow G_0 , but is rather dominated by other factors. Fig. 11 also demonstrates that PAHs compete much better for FUV photons in the diffuse ISM than in compact H II regions. This may reflect the destruction of PAHs inside the ionized gas volume since dust can be present inside H II regions (Martín-Hernández et al. 2003) and thereby absorb much of the FUV flux before it even reaches the surrounding PAH-rich PDRs. In this case, the importance of this PAH destruction in the ionized gas will increase with decreasing size of the H II region because this corresponds to a larger dust optical depth in the ionized gas for a given dust abundance and hence absorb more of the FUV flux. Possibly, the observed large spread in the 6.2PAH/FIR ratio with G_0 reflects the variation in the internal dust content of H II regions. It is fair to say, however, that at this point the origin of the large variation in the 6.2PAH/FIR ratio is unclear.

5.2. PAHs as a tracer of star formation

Star formation properties of galaxies are essential in assessing their evolutionary histories. Different tracers for star formation are used based upon integrated colors, the UV continuum, recombination and forbidden lines and FIR emission (e.g. Kennicutt 1998, and references therein). PAHs may also provide a convenient tracer of star formation activity as Sect. 4 exemplifies. PAHs are stochastically heated mainly by UV photons produced by massive stars (PAHs can also be excited by visual photons, though the excitation is dominated by UV photons, e.g. Uchida et al. 1998; Li & Draine 2002). Assuming fixed emission and absorption properties and fixed PAH abundance, the PAH emission is a measure of the amount of photons available between 6 and 13.6 eV (the former corresponding with the averaged ionization potential of PAHs) and hence of star formation. However, using the PAH emission as a tracer of star formation activity is wrought with difficulty as Sect. 5.1 illustrates; i.e. the 6.2PAH/FIR varies over 2 orders of magnitude for Galactic H II regions in our sample. To assess the robustness of this tracer, we compared it to other star formation tracers, N_{Iyc} and L_{FIR} , both for Galactic star forming regions and galaxies (normal and starbursts).

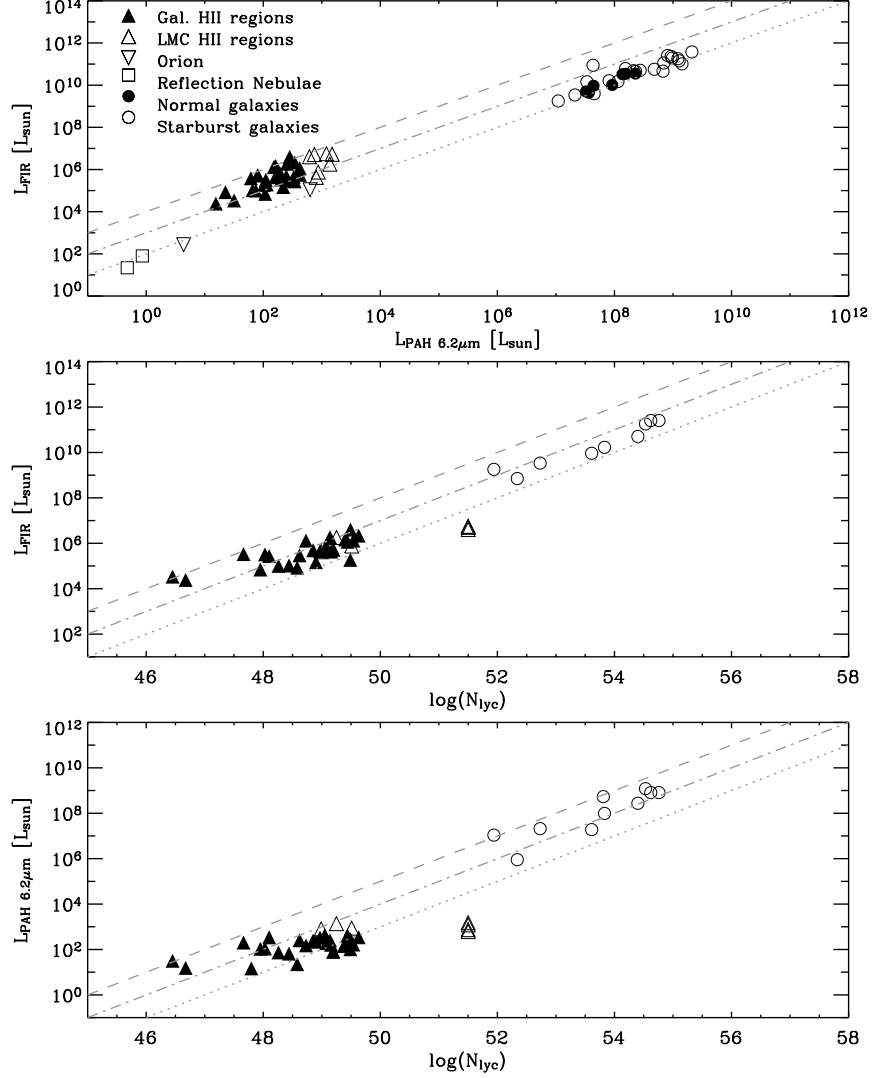


Fig. 12.— Three tracers of star formation, $L_{6.2PAH}$, $\log(N_{lyc})$ and L_{FIR} plotted against each other for Galactic H II regions, LMC H II regions (Vermeij et al. 2002) and normal and starburst galaxies. In case of a distance ambiguity for the Galactic H II regions, only the far distance is shown. The *grey lines* (*dotted*, *dash-dotted*, *dashed*) indicate a $L_{6.2PAH}$ equal to respectively 1, 0.1 and 0.01 % of L_{FIR} (**top panel**), a N_{lyc}/L_{FIR} ratio of respectively 10^{44} , 10^{43} and 10^{42} (**middle panel**) and a $N_{lyc}/L_{6.2PAH}$ ratio of respectively 10^{47} , 10^{46} and 10^{45} (**bottom panel**).

L_{FIR} traces star formation since a significant fraction of the stellar radiation is emitted by (young) stars with spectral types mid-B or earlier and is absorbed by dust and re-emitted thermally in the FIR. Also, the number of ionizing photons, N_{lyc} , is commonly used as a measure of massive star formation. It is mainly derived in three ways, 1) from the $\text{H}\alpha$ recombination line; 2) from radio recombination lines and 3) from the hydrogen free-free continuum emission at radio wavelengths. For our Galactic and LMC H II regions, N_{lyc} is obtained from radio continuum emission (Martín-Hernández et al. 2002, 2003; Vermeij et al. 2002). For our galaxies, free-free radio emission may be contaminated with non-thermal synchrotron emission from young SNR or AGN activity. Their N_{lyc} is therefore obtained from near- and mid-IR hydrogen recombination lines instead (Genzel et al. 1998; Verma et al. 2003; Förster Schreiber et al. 2001).

L_{FIR} is in first order (on this scale – within a factor of 100) clearly linearly proportional to $L_{6.2\text{PAH}}$ (Fig. 12). However, their ratio is significantly different between the Galactic H II regions ($5.5 \pm 4.6 \cdot 10^{-4}$) and the galaxies ($6.3 \pm 3.2 \cdot 10^{-3}$), with Orion and the RNe having a similar and lower ratio as the galaxies, respectively (also seen in Figs. 4 through 8). In contrast, this discrepancy between the Galactic and extragalactic sample is not present in the $L_{\text{FIR}}/N_{\text{lyc}}$ ratio, though a slightly larger scatter is observed in each of these groups (Fig. 12). In addition, $L_{6.2\text{PAH}}$ is roughly proportional to N_{lyc} for the galaxies (consistent with Roussel et al. 2001) while for the Galactic H II regions, it is much less dependent on N_{lyc} (Fig. 12). In fact, the $L_{6.2\text{PAH}}$ observed in H II regions seems to be almost independent of the hardness of the radiation field.

As discussed by e.g. Kennicutt (1998), and references therein, the robustness of L_{FIR} as a tracer for star formation depends on the type of galaxies considered, being highest for dusty circumnuclear starbursts. Indeed, the FIR spectra of galaxies are composed of emission of dust around young star-forming regions and emission of more extended dust heated by the interstellar radiation field. The same holds for PAHs as a tracer of star formation. Likewise, the observed PAH flux is integrated over the whole galaxy and therefore also includes PAH emission originating in the ISM, RNe, exposed PDRs and embedded compact H II regions. This ISM contribution can be estimated by comparing $L_{6.2\text{PAH}}$ with N_{lyc} (since it does not suffer from this contamination) for both the H II regions — as a template for massive star formation — and the galaxies. Concerning L_{FIR} , the galaxies show a similar distribution of $N_{\text{lyc}}/L_{\text{FIR}}$ as the H II regions (Fig. 13) and so L_{FIR} is likely not influenced by an ISM contribution in these galaxies. In contrast, the galaxies have a clearly different distribution in $N_{\text{lyc}}/L_{6.2\text{PAH}}$ compared to the H II regions, with — on average — a lower ratio, indicating that the PAH emission in galaxies partly originates in the ISM. Therefore, PAHs do not trace massive star formation (O stars; consistent with Haas et al. 2002) and may be better suited as a tracer of B stars, which dominate the Galactic stellar energy budget. Obviously,

PAHs are a bad tracer for highly embedded massive star formation due to their absence in the MIR spectrum of these objects.

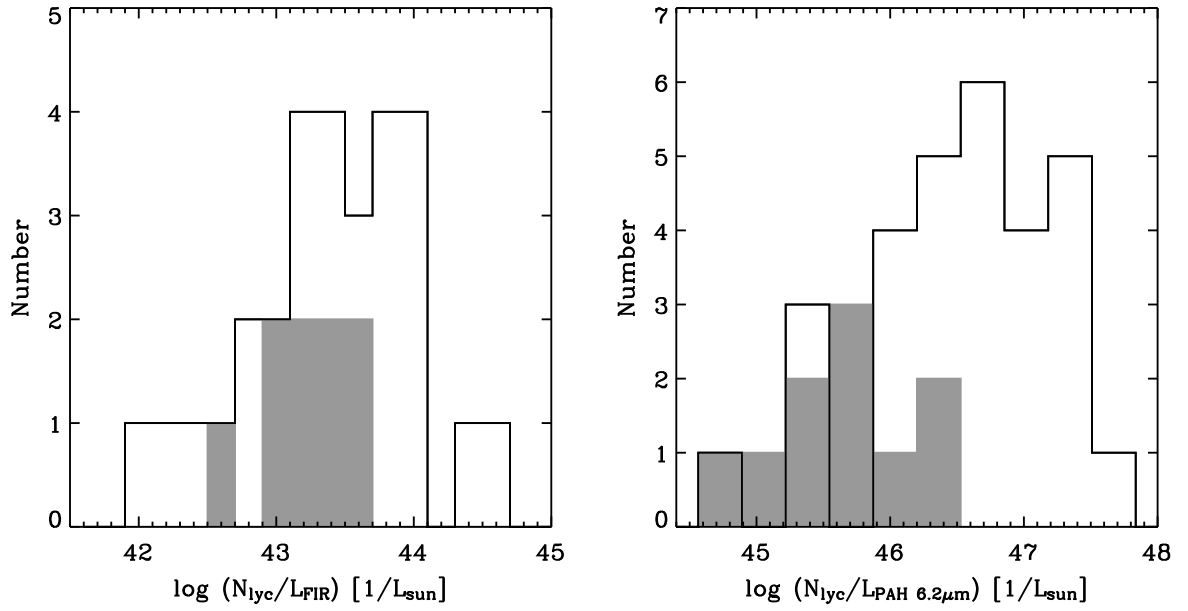


Fig. 13.— The distributions in $N_{\text{lyc}}/L_{\text{FIR}}$ and $N_{\text{lyc}}/L_{6.2\text{PAH}}$ for the Galactic and LMC H II regions (*solid line*) and the normal and starburst galaxies (*grey scale*).

5.3. Conversion from PAH luminosity to IR luminosity

Recently, Soifer et al. (2002) and Lutz et al. (2003) have used PAH emission as a quantitative measure for the contribution of exposed star formation to the bolometric luminosity of two ULIRGs (Arp 220 and NGC 6240). While Soifer et al. (2002) assumed the ratio of $L(11.2\text{PAH})$ and $L(\text{IR})$ for the starburst core in M 82 to be a measure for exposed star formation, Lutz et al. (2003) instead used the mean $L(7.7\text{PAH})/L(\text{IR})$ ratio derived from a sample of 10 starburst nuclei. A third method to derive the bolometric correction was proposed in Spoon et al. (2004) and is based on the mean $L(6.2\text{PAH})/L(\text{IR})$ ratio for our sample of normal and starburst nuclei. This ratio is $3.4 \pm 1.7 \times 10^{-3}$.

For sources where the environment of massive star formation resembles exposed PDRs (such as M 82 and NGC 253; Carral et al. 1994; Lord et al. 1996), the three methods discussed above will give reasonable results. On the other hand, for sources which resemble embedded star formation (e.g. Arp 220 and NGC 4418), a ten times lower ratio, appropriate for compact H II regions like W3, might be a better choice. Which conversion ratio is more appropriate cannot be decided based upon the mid-IR spectra alone. Observations of PDR lines such as the $[\text{O I}] 63 \mu\text{m}$ and $[\text{C II}] 158 \mu\text{m}$ lines can be very instrumental in resolving this issue. In that respect, we note that the PDR fine structure lines are very weak in Arp 220 and other ULIRGs (Luhman et al. 2003; Dale et al. 2004), suggesting also that the PDR component is underdeveloped, perhaps due to absorption of a major fraction of the FUV flux by dust inside the H II region (Luhman et al. 2003).

6. Conclusions

In this paper, the MIR spectral characteristics of Galactic and extragalactic sources are investigated. Our sample includes Galactic (C)H II regions, ISM lines of sight and embedded massive protostars as well as normal galaxies, starburst galaxies, Seyferts, QSOs and (ultra-luminous) IR galaxies.

First, the MIR spectrum of each object type is described and compared, revealing distinct spectral characteristics for each object type. In order to distinguish the different natures of the galaxies, i.e. AGN-dominated, starburst-dominated or heavily obscured, we present a new MIR/FIR diagnostic based on the ratio of the 6.2 PAH emission band to FIR flux and the ratio of the $6.2 \mu\text{m}$ continuum to FIR flux. This diagnostic is also applied to our Galactic sample. Both ratios vary clearly within our sample of H II regions and this range extends up to the RNe and the (diffuse) ISM lines of sight. In addition, the $6.2\text{PAH}/6.2\text{cont}$ ratio varies slightly over a wide range of Galactic H II regions, as well as more general

ISM material. However, the observed variation in Galactic sources is much smaller than that in galaxies. As such, it provides a very clear handle on any AGN contribution to the MIR. Indeed, AGNs are found to segregate in two groups; most Sf2s are located with the normal and starburst galaxies, while most Sf1s show strong 6.2cont/FIR ratios. The 6.2 μm PAH luminosity distributions are found to be independent of the Seyfert type, in accordance with the orientation dependent AGN unification scheme, and hence confirm the results of Clavel et al. (2000). This diagram further reveals the spectral resemblance of starburst and normal galaxies to exposed PDRs rather than (slightly embedded) compact H II regions. ULIRGs show a diverse spectral appearance. Some show a typical AGN hot dust continuum. More, however, are either starburst-like or show signs of strong dust obscuration in the nucleus. One characteristic of the ULIRGs seems also to be the presence of more prominent FIR emission than either starburst galaxies or AGNs. Comparison with the diagnostic diagrams proposed by Genzel et al. (1998) and Laurent et al. (2000) for our sample (both Galactic and extragalactic) indicates that the ability to identify obscured objects is best achieved with our MIR/FIR diagnostic, while the ability to identify the presence of an optically-recognized AGN is best achieved with the Genzel diagram.

We found that the observed variation of the MIR/FIR diagnostic ratios in the Galactic sample is linked with their evolutionary state and the PAH/dust abundance. Finally, we have examined the use of PAHs as quantitative tracers of star formation activity and find that PAHs may be better suited as a tracer of B stars, which dominate the Galactic stellar energy budget, than as a tracer of massive star formation. Likewise, the PAH emission of normal and starburst galaxies is best represented by that of exposed PDRs such as the Orion Nebula. However, the IR spectra of some sources — notably the archetypal ULIRG Arp 220 — may be dominated by embedded massive star formation rather than exposed PDRs.

We thank D. Lutz and the anonymous referee for useful comments and W.Reach, S.Madden and J.P.Simpson for providing spectra. This research is based on observations with ISO, an ESA project with instruments funded by ESA Member States (especially the PI countries: France, Germany, the Netherlands and the United Kingdom) and with the participation of ISAS and NASA. This research has made use of the NASA/IPAC Extragalactic Database (NED), operated by the Jet Propulsion Laboratory, California Institute of Technology, under contract with the National Aeronautics and Space Administration.

REFERENCES

Allamandola L.J., Tielens A.G.G.M., Barker J.R., 1985, *ApJ Lett.* 290, L25

- Allamandola L.J., Tielens A.G.G.M., Barker J.R., 1989, *Naps* 71, 733
- Antonucci R., 1993, *ARA&A* 31, 473
- Bakes E.L.O., Tielens A.G.G.M., Bauschlicher C.W., 2001a, *ApJ* 556, 501
- Bakes E.L.O., Tielens A.G.G.M., Bauschlicher C.W., Hudgins D.M., Allamandola L.J., 2001b, *ApJ* 560, 261
- Boulanger F., Abergel A., Bernard J.P., et al., 1998a, In: *ASP Conf. Ser. 132: Star Formation with the Infrared Space Observatory*, p. 15
- Boulanger F., Cox P., Jones A., 1998b, In: *a NATO Advanced Study Institute Les Houches, session LXX, Infrared Space Astronomy, today and tomorrow*, p. 251
- Boulanger F., Reach W.T., Abergel A., et al., 1996, *A&A* 315, L325
- Bregman J., Temi P., 2004, *A&A*, submitted
- Carral P., Hollenbach D.J., Lord S.D., et al., 1994, *ApJ* 423, 223
- Casey S.C., 1991, *ApJ* 371, 183
- Cesarsky D., Jones A.P., Lequeux J., Verstraete L., 2000, *A&A* 358, 708
- Charmandaris V., Laurent O., Mirabel I.F., et al., 1999, *Ap&SS* 266, 99
- Chrysostomou A., Brand P.W.J.L., Burton M.G., Moorhouse A., 1992, *MNRAS* 256, 528
- Clavel J., Schulz B., Altieri B., et al., 2000, *A&A* 357, 839
- de Graauw T., Haser L.N., Beintema D.A., et al., 1996, *A&A* 315, L49
- Contursi A., Lequeux J., Hanus M., et al., 1998, *A&A* 336, 662
- Dale, D. A., Helou, G., Brauher, J. R., et al., 2004, *ApJ* 604, 565
- Evans A.S., Becklin E.E., Scoville N.Z., et al., 2003, *AJ* 125, 2341
- Förster Schreiber N.M., Genzel R., Lutz D., Kunze D., Sternberg A., 2001, *ApJ* 552, 544
- Genzel R., Lutz D., Sturm E., et al., 1998, *ApJ* 498, 579
- Gerakines P.A., Whittet D.C.B., Ehrenfreund P., et al., 1999, *ApJ* 522, 357
- Giard M., Bernard J.P., Dennefeld M., 1992, *A&A* 264, 610

- Giard M., Bernard J.P., Lacombe F., Normand P., Rouan D., 1994, *A&A* 291, 239
- Graham J.R., Serabyn E., Herbst T.M., et al., 1993, *AJ* 105, 250
- Guainazzi M., Matt G., Brandt W.N., et al., 2000, *A&A* 356, 463
- Haas, M., Klaas, U., Bianchi, S., 2002, *A&A* 385, L23
- Helou G., Lu N.Y., Werner M.W., Malhotra S., Silbermann N., 2000, *ApJ Lett.* 532, L21
- Henning T., Klein R., Launhardt R., Lemke D., Pfau W., 1998, *A&A* 332, 1035
- Hony S., Van Kerckhoven C., Peeters E., et al., 2001, *A&A* 370, 1030
- Iwasawa K., Koyama K., Awaki H., et al., 1993, *ApJ* 409, 155
- Joblin C., Abergel A., Bregman J., et al., 2000, *ISO beyond the peaks: The 2nd ISO workshop on analytical spectroscopy. Eds. A. Salama, M.F.Kessler, K. Leech & B. Schulz. ESA-SP* 456, 49
- Joblin C., Tielens A.G.G.M., Allamandola L.J., Geballe T.R., 1996, *ApJ* 458, 610
- Kahanpää J., Mattila K., Lehtinen K., Leinert C., Lemke D., 2003, *A&A* 405, 999
- Kennicutt R.C., 1998, *ARA&A* 36, 189
- Kessler M.F., Steinz J.A., Anderegg M.E., et al., 1996, *A&A* 315, L27
- Laureijs R.J., Watson D., Metcalfe L., et al., 2000, *A&A* 359, 900
- Laurent O., Mirabel I.F., Charmandaris V., et al., 2000, *A&A* 359, 887
- Léger A., Puget J.L., 1984, *A&A* 137, L5
- Li, A., Draine, B. T., 2002, *ApJ*, 572, 232
- Lord S.D., Hollenbach D.J., Haas M.R., et al., 1996, *ApJ* 465, 703
- Luhman M.L., Satyapal S., Fischer J., et al., 2003, *ApJ* 594, 758
- Lu N., Helou G., Werner M. W., et al., 2003, *ApJ* 588, 199
- Lutz, D. and Feuchtgruber, H. and Genzel, R., et al., 1996, *A&A* 315, L269
- Lutz D., Spoon H.W.W., Rigopoulou D., Moorwood A.F.M., Genzel R., 1998, *ApJ Lett.* 505, L103

- Lutz, D., 1999, In: *ESA SP-427: The Universe as Seen by ISO*, vol. 427, 623
- Lutz D., Sturm E., Genzel R., et al., 2003, *A&A* 409, 867
- Malhotra S., Kaufman M.J., Hollenbach D., et al., 2001, *ApJ* 561, 766
- Martín-Hernández N.L., Peeters E., Morisset C., et al., 2002, *A&A* 381, 606
- Martín-Hernández N.L., van der Hulst J.M., Tielens A.G.G.M., 2003, *A&A* 407, 957
- Mattila K., Lehtinen K., Lemke D., 1999, *A&A* 342, 643
- Meixner M., Haas M.R., Tielens A.G.G.M., Erickson E.F., Werner M., 1992, *ApJ* 390, 499
- Mirabel I.F., Vigroux L., Charmandaris V., et al., 1998, *A&A* 333, L1
- Moutou C., Sellgren K., Léger A., Verstraete L., Le Coupanec P., 1999a, In: d’Hendecourt L., Joblin C., Jones A. (eds.), *Solid Interstellar Matter : The ISO Revolution*, EDP Sciences, 90
- Moutou C., Verstraete L., Sellgren K., Léger A., 1999b, In: *ESA SP-427: The Universe as Seen by ISO*, vol. 427, 727
- Onaka T., 2000, *Advances in Space Research* 25, 2167
- Onaka T., Yamamura I., Tanabe T., Roellig T.L., Yuen L., 1996, *PASJ* 48, L59
- Peeters E., Allamandola L.J., Hudgins D.M., Hony S., Tielens A.G.G.M., 2004, In: Witt A.N. (ed.), *Astrophysics of Dust*, Astronomical Society of the Pacific, vol. CS-309
- Peeters E., Hony S., Van Kerckhoven C., et al., 2002a, *A&A* 390, 1089
- Peeters E., Martín-Hernández N.L., Damour F., et al., 2002b, *A&A* 381, 571
- Puget J.L., Léger A., 1989, *ARA&A* 27, 161
- Reach W.T., Boulanger F., Contursi A., Lequeux J., 2000, *A&A* 361, 895
- Rigopoulou D., Spoon H.W.W., Genzel R., et al., 1999, *AJ* 118, 2625
- Risaliti G., Elvis M., Nicastro F., 2002, *ApJ* 571, 234
- Roelfsema P.R., Cox P., Tielens A.G.G.M., et al., 1996, *A&A* 315, L289
- Roussel H., Sauvage M., Vigroux L., Bosma A., 2001, *A&A* 372, 427

- Sanders D.B., Mirabel I.F., 1996, *ARA&A* 34, 749
- Sellgren K., Tokunaga A.T., Nakada Y., 1990, *ApJ* 349, 120
- Simpson J.P., Witteborn F.C., Price S.D., Cohen M., 1998, *ApJ* 508, 268
- Soifer B.T., Neugebauer G., Matthews K., Egami E., Weinberger A.J., 2002, *AJ* 124, 2980
- Spoon H.W.W., Keane J.V., Tielens A.G.G.M., Lutz D., Moorwood A.F.M., 2001, *A&A* 365, L353
- Spoon H.W.W., Keane J.V., Tielens A.G.G.M., et al., 2002, *A&A* 385, 1022
- Spoon H.W.W., Koornneef J., Moorwood A.F.M., Lutz D., Tielens A.G.G.M., 2000, *A&A* 357, 898
- Spoon H.W.W., Moorwood A.F.M., Lutz D., et al., 2004, *A&A* 414, 873
- Steiman-Cameron T.Y., Haas M.R., Tielens A.G.G.M., Burton M.G., 1997, *ApJ* 478, 261
- Sturm E., Lutz D., Tran D., et al., 2000, *A&A* 358, 481
- Sturm E., Lutz D., Verma A., et al., 2002, *A&A* 393, 821
- Thronson H.A., Harper D.A., 1979, *ApJ* 230, 133
- Thronson H.A., Harper D.A., Bally J., et al., 1986, *AJ* 91, 1350
- Thronson H.A., Harper D.A., Smith H.A., et al., 1984, In: *Airborne Astronomy Symposium*, 127
- Tielens A.G.G.M., Meixner M.M., van der Werf P.P., et al., 1993, *Sci* 262, 86
- Tielens A.G.G.M., Hony S., Van Kerckhoven C., Peeters E., 1999, In: *ESA SP-427: The Universe as Seen by ISO*, vol. 427, 579
- Tielens A.G.G.M., van Kerckhoven C., Peeters E., Hony S., 2000, In: *Astrochemistry: From Molecular Clouds to Planetary*, vol. 197, 349
- Tran Q.D., Lutz D., Genzel R., et al., 2001, *ApJ* 552, 527
- Uchida, K. I. and Sellgren, K. & Werner, M., *ApJL*, 493, L109
- van Diedenhoven B., Peeters E., Van Kerckhoven C., et al., 2004, *ApJ* submitted
- Van Kerckhoven C., Hony S., Peeters E., et al., 2000 *A&A* 357, 1013

- Veilleux S., Osterbrock D.E., 1987, *ApJS* 63, 295
- Verma A., Lutz D., Sturm E., et al., 2003, *A&A* 403, 829
- Vermeij R., Peeters E., Tielens A.G.G.M., van der Hulst J.M., 2002, *A&A* 382, 1042
- Verstraete L., Pech C., Moutou C., et al., 2001, *A&A* 372, 981
- Verstraete L., Puget J.L., Falgarone E., et al., 1996, *A&A* 315, L337
- Werner M.W., Gatley I., Becklin E.E., et al., 1976, *ApJ* 204, 420